Laboratory Astrophysics Experiments to Study Star Formation

by

Rachel Pierson Young

A dissertation submitted in partial fulfillment
of the requirements for the degree of
Doctor of Philosophy
(Applied Physics)
in The University of Michigan
2017

Doctoral Committee:

Professor R. Paul Drake, Co-Chair
Associate Research Scientist Carolyn C. Kuranz, Co-Chair
Professor Yue Ying Lau
Associate Professor Susan T. Lepri
Professor Greg Tarle

Rachel Pierson Young

rpyoung@umich.edu

ORCID: 0000-0003-3291-6737

ACKNOWLEDGEMENTS

My path to graduate school is an unconventional one: after completing my undergraduate education I served a tour of duty in the U. S. Navy. I'm not sure I would have returned to school at all had I not had the encouragement of my undergraduate advisor, Dr. Pat Hartigan, so I ought to begin there. Thank you for helping me keep my foot in the door for those years and for giving me the idea to attend the 2008 HEDLA Conference, where I met the University of Michigan research group that I have had the pleasure of working with for my graduate education.

I would like to thank my co-advisors, Dr. Paul Drake and Dr. Carolyn Kuranz for your tireless support and advice. I would like to particularly thank Carolyn, who may not realize the impact she had on me when we met at the HEDLA conference mentioned above. She talked about how she balanced graduate school with having small children at home and it gave me confidence in the path I wanted to take.

Our research at Michigan is very much a group effort. I would like to thank the whole team of scientists, students and support staff. In particular, I ought to thank Sallee Klein and Rob Gillespie for painstakingly machining and assembling the experimental targets themselves. I would also like to single out the rest of the magnetized plasma group within CLEAR: Dr. Mario Manuel and fellow graduate student Joseph Levesque; thanks for letting me bounce ideas off you and for keeping me company on those long drives to OMEGA.

I would like to thank the rest of our collaboration outside of the University of Michigan: Dr. Pat Hartigan and graduate student Andy Liao of Rice University;

Dr. Dustin Froula, Dr. Gennady Fiksel, Dr. Po-Yu Chang, and graduate student Daniel Barnak at the Laboratory for Laser Energetics (Dr. Fiksel has since moved to the University of Michigan); Dr. Steven Ross of Lawrence Livermore National Laboratory; and Dr. Chikang Li, and graduate students Hong Sio and Alex Zylstra of Massachusetts Institute of Technology (Alex Zylstra has graduated and moved to Los Alamos National Laboratory since his work on this collaboration). Additionally, I would like to thank the entire engineering and support staff of the Laboratory for Laser Energetics for making my OMEGA shot days run so smoothly.

I would like to thank my parents, Robert and Vicki, for raising me to have a questioning mind, and my sister, Julia, for keeping my spirits up with her sense of humor when I was bogged down with writing or experiments.

I would not be where I am today without the loving support of my husband, Steve. Steve, thank you for always believing in me and for holding down the fort when I was out of town for experiments. You have made so many sacrifices from the small to the large to the estimated 28 feet of snow you've shoveled since you moved to Ann Arbor (at my behest). I don't think I will ever be able to repay you.

Finally, my little boys, Ike and Jay, have not been especially helpful, but they have been an enormous joy. In fairness, Ike did attempt to help me by writing my thesis for me (see next page), but I suspect it would not pass muster with the Rackham thesis formatting department.

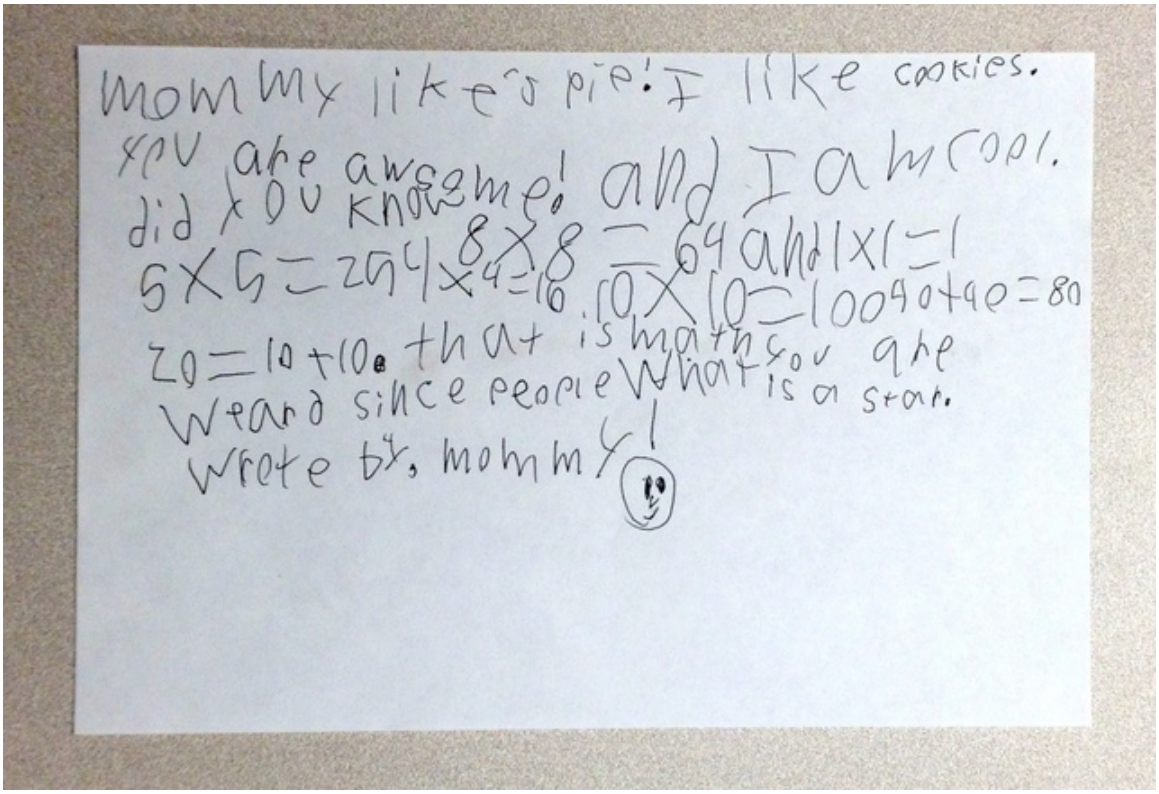
mommy likes pie! I like cookies.
you are awesome! and I am cool.
did you know 8 x 8 = 64 and 1 x 1 = 1
5 x 5 = 25 4 x 4 = 16 10 x 10 = 100 40 + 40 = 80
20 = 10 + 10 that is maths you are
weird since people what is a star.
wrote by, mommy

TABLE OF CONTENTS

LIST OF FIGURES

Figure

LIST OF TABLES

Table

LIST OF APPENDICES

Appendix

ABSTRACT

Laboratory Astrophysics Experiments to Study Star Formation

by

Rachel Pierson Young

Co-chairs: R. Paul Drake and Carolyn C. Kuranz

As a thesis project, I devised and implemented a scaled accretion shock experiment on the OMEGA laser (Laboratory for Laser Energetics). This effort marked the first foray into the growing field of laser-created magnetized flowing plasmas for the Center for Laser Experimental Astrophysical Research (CLEAR) here at the University of Michigan.

Accretion shocks form when streams of accreting material fall to the surface of a young, growing star along magnetic field lines and, due to their supersonic flow, create shocks. As I was concerned with what was happening immediately on the surface of the star where the shock forms, I scaled the system by launching a plasma jet (the accreting flow) and driving it into a solid surface (the stellar surface) in the presence of an imposed magnetic field parallel to the jet flow (locally analogous to the dipole field of the star).

Early work for this thesis project was dedicated to building a magnetized flowing plasma platform at CLEAR. I investigated a method for launching collimated plasma jets and studied them using Thomson scattering, a method which measures parameters such as temperature and density by scattering a probe beam off the experimental

plasma. Although the data were corrupted with probe heating effects, I overcame this problem by finding the mass density of the jets and using it to determine they were isothermal rarefactions with a temperature of 6 eV.

Scaling an astrophysical phenomenon to the laboratory requires tailoring the parameters of the experiment to preserve its physics, rather than creating an experiment that merely superficially resembles it. I ensured this by distilling the driving physical processes of the astrophysical system—accretion shocks—into a list of dimensionless number constraints and mapping these into plasma parameter space.

Due to this project being the first magnetized flowing plasma effort at CLEAR, it suffered the growing pains typical of a young research program. Of my two primary diagnostics for the accretion shock experiment, visible light imaging was successful, but proton radiography, which was intended to probe magnetic field structure, failed twice for two independent reasons. The visible light data show that a shock forms and grows rapidly. However, there are no observable structural differences between the magnetized and un-magnetized shots. It may be that there were subtle structural differences that would have been evident in proton radiographs but did not appear in visible light images.

However, it may also be that the magnetic field was not strong enough to affect the structure; given the plasma and magnetic field parameters of the shot day, the experiment was analogous to a young star with a magnetic field of 325 Gauss, which is weaker than the roughly 1 kilo-Gauss fields typically observed. If this experimental effort continues after my departure, it would benefit from making use of one of the novel low-density plasma stream generation techniques being developed at CLEAR.

CHAPTER I

Introduction

1.1 Overview

While a scaled experimental version of a complicated system might seem a poor substitute for the real thing, it offers researchers several advantages: it can be tested under controlled conditions, altered easily, and fine-tuned to reveal insights in the basic physics of the system. The scaled experiments the general public is most familiar with are model aircraft tested in wind tunnels. What the general public may not be aware of is that wind tunnels predate flight by more than thirty years; the Wright brothers' historic accomplishment at Kitty Hawk would not have been possible without a generation of researchers investigating the basic physics of flight in a scaled setting.

This thesis pertains to a different sort of scaled experiments, high-energy laser experiments which are scaled to astrophysical systems. Conceptually, scaling an astrophysical system is similar to scaling an aircraft: it is an attempt to make a smaller version of the real thing that preserves its physics and thus will tell the researcher something useful about the system of interest. But model aircraft are only scaled down by two or three orders of magnitude in size, while an astrophysical system might be scaled down by ten or more orders of magnitude. Moreover, some astrophysical phenomena, such as gravitation, cannot be reproduced in the laboratory.

Scaling an astrophysical system, therefore, requires choices and tradeoffs: what are the most important physical processes of the astrophysical system and how might they be reproduced—or approximated—in a laboratory setting?

Fluid dynamicists have long used dimensionless numbers to distill the behavior of a fluid system down to its essentials. To return to the model aircraft example above, a researcher wishing to test a model wing in an wind tunnel would adjust the air flow such that the Reynolds number[1] of the wind tunnel system matched the Reynolds number expected when the actual aircraft took flight. This basic process—fiddling with experimental parameters to make dimensionless numbers line up—is what researchers mean when they say a system is "well-scaled."

For my thesis project, I designed and implemented a laser experiment which I argue is well-scaled version of an accretion shock. Accretion shocks form in any accreting system; I focused on those that occur during star formation at the surfaces of young, growing stars. All stars form at the center of accretion disks, see Figure 1.1. The most widely accepted accretion model is magnetospheric accretion, wherein the magnetic field of the young star is thought to control the accretion process, lifting material out of the plane of the disk and funneling it to the stellar surface along magnetic field lines. When the accreting material impacts at the surface of the star, it creates a shock. From the perspective of a local observer on the surface of the star, it would appear that accreting material was falling to the surface along field lines that ran perpendicular to the surface (that is, up and down).

It was this specific part of the star formation process that I decided to scale to laboratory experiment, see Figure 1.2. In the astrophysical system, a stream of accreting material flows down along stellar magnetic field lines, impacts at the stellar surface, and forms a shock. In the laboratory experiment, a plasma jet (the "accreting flow") is driven into a solid surface (the "stellar surface") in the presence of an imposed

[1]The Reynolds number captures the importance of viscous effects.

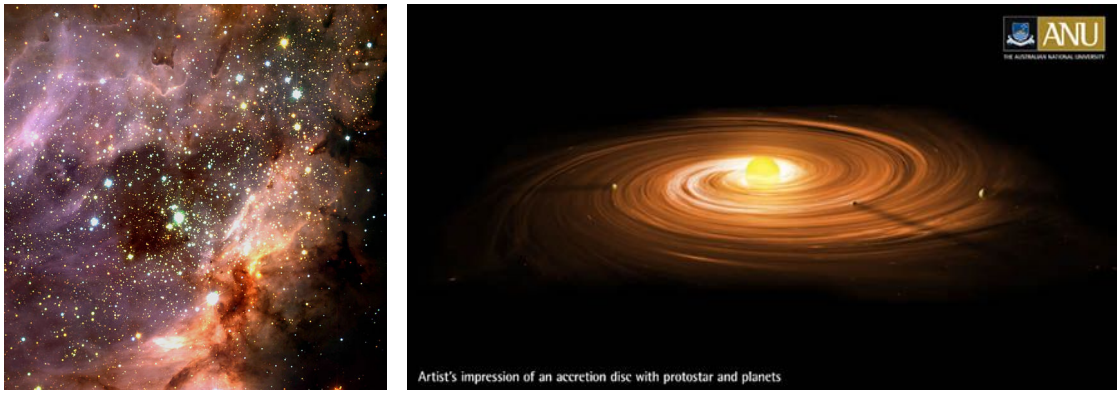

Figure 1.1: The star forming region M17 (left) and an artist's conception of a young star system (right). (Image credit: left, European Southern Observatory, and right, Australian National University.)

magnetic field that runs parallel to the flow (analogous to the local field of the star). To argue that the experiment was well-scaled, I tailored the plasma conditions of the experiment to make a dimensionless-number-based scaling argument.

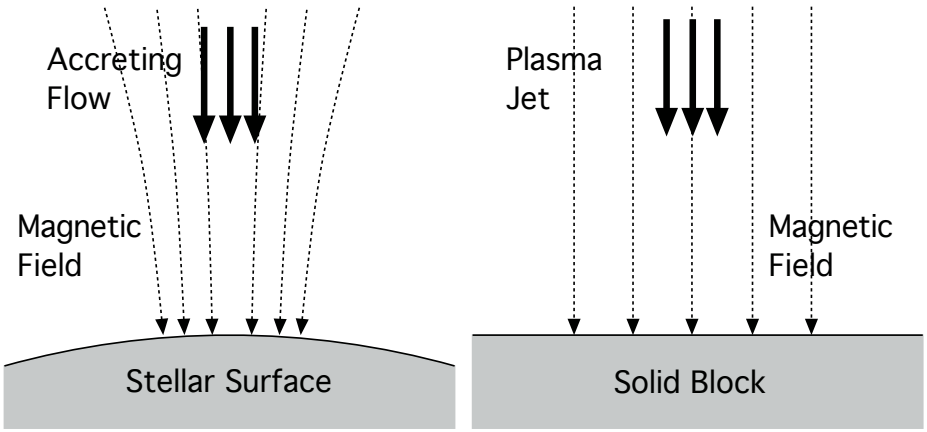

Figure 1.2: Diagram of the astrophysical and laboratory accretion shock systems. In the astrophysical system (left), accreting plasma falls to the stellar surface along magnetic field lines. This is translated into a laboratory experiment (right) by driving a jet into a block in an imposed magnetic field.

The primary objective of this project was to investigate the role of the magnetic field in the structure and evolution of accretion shocks. Based on existing astrophysical simulation work, I hypothesized that magnetic fields would play a crucial role in the structure of the post-shock material. I expected a strong field to trap the shock

in a tight column of post-shock material, whereas a weak field would fail to contain it, and it would splash out to the sides, much like a stream of water does when it hits a surface.

1.2 Laboratory Astrophysics

My work in laboratory astrophysics stands on the shoulders of nearly twenty years of work in scaling astrophysical systems to laboratory experiments with dimensionless numbers (*Ryutov et al.*, 1999; *Remington et al.*, 2000, 2006). This project was conducted under the auspices of The Center for Laser Experimental Astrophysical Research (CLEAR). CLEAR is based at the University of Michigan and is lead in part by my co-advisors, Paul Drake and Carolyn Kuranz. Examples of laboratory astrophysics work previously conducted by CLEAR and its predecessor include the work of *Kuranz et al.* (2009), who created Rayleigh-Taylor blast waves relevant to supernovae remnants; and the work of *Krauland et al.* (2013), who created reverse shocks relevant to interacting binaries.

This section will lay out hydrodynamic/magnetohydrodynamic (MHD) laboratory astrophysics work in the sub-field of star formation. As related in the last section, stars form at the center of accretion disks; these star-disk systems are accompanied by bipolar jets that extend several light-years into the interstellar medium. Most star-formation-related laboratory astrophysics focuses on the launch mechanism and their structure of these jets. In addition to the wealth of experiments aimed at exploring jet behavior, there are several studies of accretion disk behavior and one other experimental team studying accretion shocks.

1.2.1 MHD Jets on MAGPIE

For over fifteen years, the Plasma Physics group at Imperial College London has lead an effort to study astrophysically relevant jets on MAGPIE, a large pulsed-power

generator. Pulsed-power devices such as MAGPIE create experimental plasmas by discharging high current through some array of conductors (wires or thin metal foils), completely vaporizing them. *Lebedev et al.* (2002) devised a new way to create plasma jets that could be relevant for laboratory astrophysics: they used a conical array of wires to launch a collimated plasma jet with velocity of $\sim 200\,\mathrm{km\,s^{-1}}$ and a Mach number of ~ 20. They found that higher Z materials had more radiative cooling and produced tighter jets. These jets became the basis for later work, including launching a conical-wire MAGPIE jet into a cross wind analogous to an astrophysical jet encountering background movement in the interstellar medium (*Lebedev et al.*, 2004).

In 2005, *Lebedev et al.* built off the conical-wire idea to develop a platform that has been the basis for over a decade of work. They substituted a flat radial array of wires for the conical array. When MAGPIE fires, the wires are completely vaporized, producing a magnetic tower above the wires with a toroidal magnetic field inside. The toroidal field compresses plasma within the bubble into a jet along the axis. The tower grows with time until the jet inside finally breaks free. These jets are radiatively cooled (cooling parameter ~ 1) and resultantly have very high Mach numbers (~ 30) (*Lebedev et al.*, 2005b). *Ciardi et al.* (2007) sent such jets into a background plasma in a jet-encounters-interstellar-medium experiment similar to that of (*Lebedev et al.*, 2004) earlier.

The genius of the radial-wires idea is that tweaking the experiment can make the jet episodic like an astrophysical jet. When the radial wire vaporize, they leave a small gap at the center. *Ciardi et al.* (2009) adjusted the experiment such that when the jet breaks free, the plasma is able to fill-in that gap, see Figure 1.3. This sets up conditions identical to those in place when MAGPIE originally fired and the filled-in configuration is able to "refire." Every time the experiment refires, the magnetic tower grows once more, a jet forms within it and eventually breaks free. Later *Suzuki-Vidal*

et al. (2010) replaced the radial wires with a thin circular conducting foil and achieved three to four eruptions per experiment.

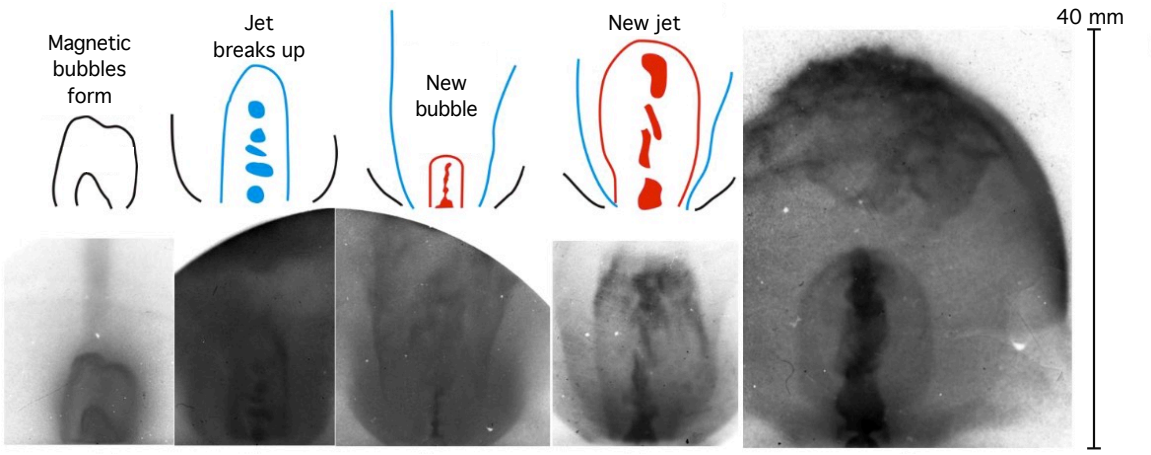

Figure 1.3: Plasma jet data from *Ciardi et al.* (2009). Over a period of roughly 200 ns, a jet forms inside a magnetic bubble, breaks up, new magnetic bubbles form, and the process repeats.

1.2.2 Jet-Obstacle Collisions on OMEGA

In 2005, *Foster et al.* began a series of experiments aimed at exploring the interaction of dense plasma jets with a surrounding medium on OMEGA, a large laser facility located at the University of Rochester. The *Foster et al.* jets (see also *Coker et al.*, 2007) were launched by irradiating a thin piece of titanium with a hohlraum, a metal cylinder which its inner walls irradiated to create a radiative cavity. The jet was collimated by a titanium washer and sent into a foam-filled cavity meant to be analogous to the interstellar medium. The resulting structures show clear bow shocks and turbulence, the same structures observed in the jets than emanate from young star systems.

While experiments that send an astrophysically relevant jet into an ambient medium are fairly common in laboratory astrophysics, the collaboration then seized on a novel variation to it: they collided their jets with polystyrene (plastic) spheres

meant to be analogous to large molecular cores in the interstellar medium (*Hartigan et al.*, 2009).

One remarkable thing about this collaboration is the lengths they have gone to to connect their laboratory results to astronomical observations and vice versa. *Hartigan et al.* (2011) used the Hubble Space Telescope to obtain time-progression data of several jets from young stars[2] and observed structures similar to those seen in the jet-foam experiments, see Figure 1.4.

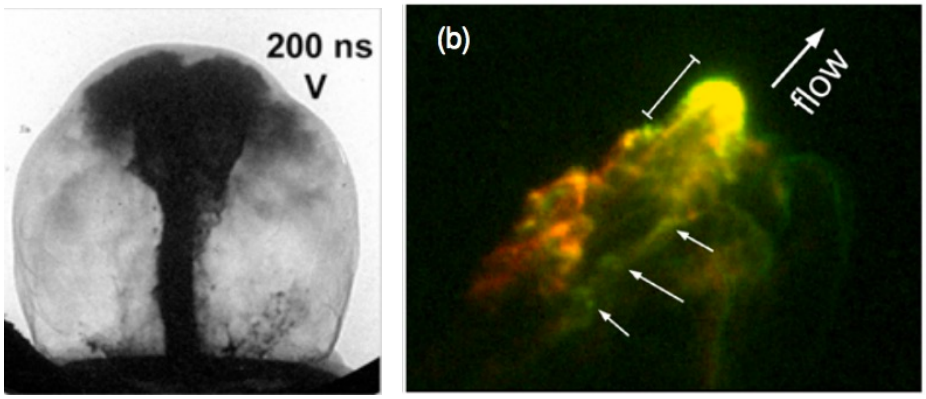

Figure 1.4: Comparison of *Hartigan et al.* (2009) experimental data (left) and *Hartigan et al.* (2011) observational data (right).

1.2.3 Jets on LULI

In 2007, *Loupias et al.* began a series of experiments that were aimed at created astrophysically relevant jets on the LULI laser at L'Ecole Polytechnique. Their experiments used an "ablator" to send a shock wave into foam. By driving the resulting foam shock through a "conical washer" (basically, a converging nozzle), they created a collimated plasma jet.

The ablator in this case was a thin piece of CH irradiated by the LULI laser. Just as a rocket is propelled forward by ejecting material out the back, irradiated material

[2]Jets from young stars are known as "Herbig-Haro objects" in honor of the scientists who originally identified them. *Hartigan et al.* (2011) observed three HH objects, HH 1, HH 34, and HH 47.

dissipating off the surface of the CH launches a shock forward through the foam. The resultant jets have Mach number of ~ 10, Reynolds number ~ 1, and Péclet number ~ 1, making them good candidates for astrophysical jet studies. The *Loupias et al.* jets were later launched into an ambient medium of argon meant to be analogous to a jet erupting into the interstellar medium (*Gregory et al.*, 2010; *Loupias et al.*, 2009).

1.2.4 MHD Jet Launching at CalTech

In the memorably titled *Why current-carrying magnetic flux tubes gobble up plasma and become thin as a result*, *Bellan* (2003) proposed that MHD pumping explains an array of phenomenon in the Universe. In *You et al.* (2005), the collaboration states their concept thusly, "an MHD force resulting from the flared current profile drives axial plasma flows along the flux tube; the flows convect frozen-in magnetic flux from strong magnetic field regions to weak magnetic field regions; flow stagnation then piles up this embedded magnetic flux, increasing the local magnetic field and collimating the flux tube via the pinch effect."

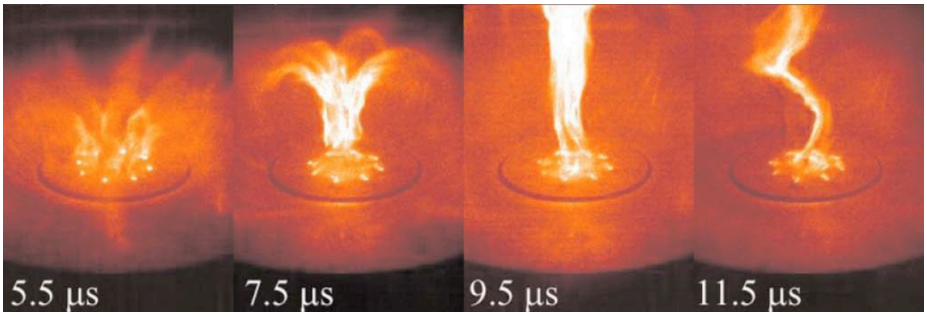

Figure 1.5: Evolution of an astrophysically relevant jet made with the Caltech plasma gun (*Bellan et al.*, 2009).

Since they proposed these ideas, this team has performed numerous experiments using the Caltech plasma gun (*Yun and Bellan*, 2010). Unlike the other jet experiments discussed in this section, these experiments are envy-inducingly large, reaching 20 cm or more, and the results resemble astrophysical jets or solar coronal loops, see Figure 1.5. They have also experimented with sending their jets into an ambient

medium (*Moser and Bellan*, 2012).

1.2.5 Accretion Disk Instabilities

These are not plasma physics experiments but I have included them because they seek to understand star-formation-related hydrodynamic and MHD behavior. For decades, accretion disk theorists have been plagued by a very basic problem: why does disk material spiral in? The disk material must be losing angular momentum to drag forces, much in the same way satellites in low-Earth-orbit lose angular momentum due to atmospheric drag—without repositioning they would spiral in to Earth. But whereas hydrodynamic viscosity is sufficient to explain the rate at which low-Earth-orbit satellites lose angular momentum, it is insufficient to explain the angular momentum loss in an accretion disk. Instead, the leading candidate is MHD viscosity stemming from the magnetorotational instability.

Ji et al. (2006) used Taylor-Couette apparatus to a create a quasi-Keplerian rotating disk with Reynolds numbers up to 2×10^6. These experiments were not magnetic; they used water or a water/glycerol mixture. Even at such high Reynolds numbers, the flow was stable, underscoring the impossibility of explaining accretion disks without MHD.

Other teams have used Taylor-Couette apparatus (or its spherical equivalent) to pursue the the magnetorotational instability. These experiments are more complicated tham the water/glycol experiment of *Ji et al.*; they required liquid metal and an imposed magnetic field. *Sisan et al.* (2004) and *Stefani et al.* (2006) have observed the magnetorotational instability, the latter at Reynolds numbers as low as 1000, in stark contrast to the high-Reynolds-number stability of the non-magnetic system.

1.2.6 POLAR Accretion Shocks

Finally, there is one laboratory-astrophysics project that complements my own because it also pertains to accretion shocks. My work was aimed at producing a scaled version of an accretion shock on the surface of a young star and exploring the role of the surrounding magnetic field in containing the shock. The POLAR project is aimed at producing a scaled version of an accretion shock on the surface of a white dwarf[3] and exploring the growth of the resulting column of radiatively cooled post-shock material (*Bouquet et al.*, 2010; *Falize et al.*, 2012; *Busschaert et al.*, 2013). There are two crucial differences between their project and mine. First, their work uses high-Z material to produce a shock with significant radiative cooling. Second, their work relies on artificial means to collimate their "accretion shock." While actual white dwarf accretion shocks are collimated by the dwarf's intense magnetic field, the POLAR team used a shock tube to contain their experiment. Laboratory magnetic fields high enough to be analogous to a white dwarf field are simply not achievable with current technology. The first results of this effort are contained in *Cross et al.* (2016), which found that the growth of the scaled radiative accretion column matches numerical predictions.

Although the POLAR team is concerned with the growth of a radiating "accretion shock column," it does not appear that they expected to observe the famous *Chevalier and Imamura* cooling instability.[4] Their papers cite the work of *Chevalier and Imamura* (1982) in passing but make no mention of seeing the instability in a laboratory experiment. I suspect that the cooling timescale for their plasma condi-

[3]White dwarfs are late-in-life stars; our own Sun will one day be one. While all young stars experience accretion during their formation, only *binary* white dwarfs experience accretion—without captured material from a binary companion there would be nothing to accrete onto them. A sub-set of these accreting white dwarfs are known as *polar* stars, hence the clever name of the laboratory-astrophysics project.

[4]The story of the *Chevalier and Imamura* (1982) cooling instability is worth relating briefly. Within a handful of years, it was observed in numerical simulations, described by analytic predictions, and observed in the x-ray spectra of accreting white dwarfs, making it a lovely example of numeric simulations actually leading the way in astrophysics.

tions was too long for the instability to appear in their experiment; I calculated the cooling timescale of my own experiment once and found that it was on the order 10^{-5} s—short by human standards but far to long for a field where experiments are measured in nanoseconds.

To date, there is one plausible laboratory observation of the cooling instability. *Hohenberger et al.* (2010) observed velocity oscillations in a radiatively cooled shock, which they attribute to the cooling instability. However, their experiment was intended to be a roughly scaled version of the cooling instability in supernovae remnants, not accretion shocks.

1.3 The OMEGA Laser

All of the experiments included in this project were performed on the OMEGA laser at the Laboratory for Laser Energetics (LLE) in Rochester, NY. Built in 1970 as part of the national effort to achieve fusion energy, OMEGA is a 30-kilojoule 60-beam frequency-tripled neodymium:glass (Nd:glass) laser system ideal for high-energy physics investigations (*Soures et al.*, 1996). As the laser was designed to implode fuel capsules in fusion experiments, the beams are distributed around the target chamber isotropically (or nearly so) making OMEGA flexible to configure for non-fusion applications. It has a wavelength of 351 nm, the third harmonic (3ω) of Nd:glass (*Boehly et al.*, 1997).

While the OMEGA facility is run by its staff scientists, engineers and technicians, experimental decisions are made on a shot-to-shot basis by the visiting experimental team. It is standard practice at the Center for Laser Experimental Astrophysical Research (CLEAR) to allow the graduate student primary investigator (PI) to make these decisions, albeit with the advice of more senior scientists. The metaphor I would use is student driving: senior scientists give advice and could in theory hit the brakes if they thought it necessary, but the graduate student PI is driving the car. As a

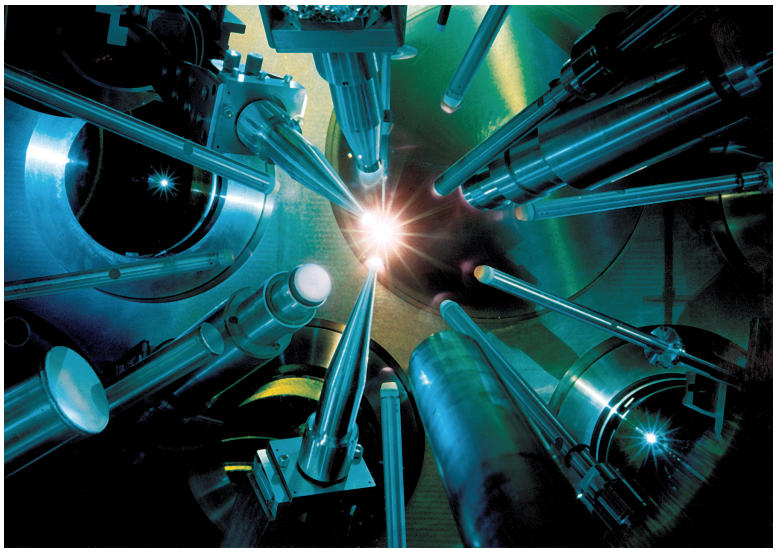

Figure 1.6: The target chamber of the OMEGA laser. (Image credit: University of Rochester).

graduate student PI, I briefed the OMEGA staff on the experiment in the morning, approved laser energy profiles, determined which configurations would be shot and what timing was needed, provided feedback to the facility on the effectiveness of each shot, and, most importantly, directed the alignment of the experimental target.

OMEGA is a remarkably flexible facility. Turn-around time between shots on OMEGA is just under an hour and experimental parameters such as timing can be altered up until a few minutes before the shot is fired. In many cases, data are available shortly after the shot, so it is possible to use the results of the previous shot to determine the course of action for the next shot. A good shot day might yield a dozen shots, so even if the shot day is going well, the primary investigator must be frugal and think critically about what pieces of data are truly crucial to answer the driving questions of the campaign.

As a graduate student PI, I was responsible for coordinating each shot day from its beginning—planning normally begins about a year in advance—to analyzing the data collected. I defined the goals of the experiment, designed targets using a computer aided design (CAD) program, and coordinated with the target fabrication team here

at the University of Michigan to have the targets built.

1.4 Description of Chapters

This thesis progresses from the motivation of the work, to early scoping studies of plasma jets, and finally to the full accretion shock experiment. The chapters are as follows:

- Chapter II discusses the process for scaling accretion shocks to a laboratory experiment. I begin with the history of our understanding of star formation, including the currently accepted models and the direct evidence of accretion shocks. I discuss how I determined the plasma conditions in astrophysical accretion shocks. I explain the dominant physics of the astrophysical accretion system and related dimensionless numbers. I enumerate the dimensionless number constraints needed to scale the system and plot each one in plasma parameter space, delineating the regions where the constraint is met and where it is not met. I conclude with two options, each of which would produce a well-scaled experiment.

- Chapter III analyzes the data obtained from collimated jet experiments in April 2012. Visible light imaging revealed that the jets were indeed collimated and that they formed easily visible shocks when collided in a head-on configuration. Thomson scattering was used to plot a mass vs. time profile for the jets, which was compared to analytic predictions. Based on those comparisons, I concluded the jets were behaving as isothermal rarefactions with $T_e \approx 6\,\mathrm{eV}$.

- Chapter IV presents the results of the accretion shock work. Unfortunately, I was not able to observe a difference between the field and no-field shots due to repeated failures of our primary diagnostic, proton radiography. However,

visible light imaging was successful and I use this to prove that we were successful in creating a shock. I relate the timing of shock formation to the scaling arguments presented in Chapter II. I also connect this work to the timing of shock formation for the collimated jet work presented in Chapter III.

- Chapter V presents all the proton radiography data. I used proton radiography for three shot day, one day devoted to a multiple jet experiment and two devoted to the accretion shock experiment. Unfortunately, proton radiography failed for both accretion shock shot days. I discuss these failures and explain the data that were obtained.

- Chapter VI presents the conclusions of this investigation and considers the future of this work. In particular, I discuss the lack of an observable difference between the field and no-field shots. This may be because proton radiography failed, but it also may be that the magnetic field was too weak to affect the flow. I consider both possibilities and their implications going forward.

- Appendix A provides background on the the OMEGA laser and the OMEGA systems used for this thesis project, which include the Magneto-Inertial Fusion Electrical Discharge System (MIFEDS), a system for imposing magnetic fields; proton radiography using a D^3He proton back-lighter, which images magnetic field structure; Thomson scattering, a technique which probes parameters such as temperature and density by scattering a probe beam off the experimental plasma; and visible light imaging, in layman's terms, taking a picture of the experiment with self-emitted radiation.

- Appendix B provides a narrative of the four shot days involved in this thesis project. Much of the effort of this project was dedicated to developing the magnetized flowing plasma platform at CLEAR and our experimental team experienced the growing pains typical of a young research program. This chap-

ter summarizes each shot day, including what was attempted, what data was gained, and what did not work as expected and resulted in a lesson learned for the next shot day.

- Each shot day has an appendix dedicated to it which contains all the data, including data that failed or was not useful.

CHAPTER II

Scaling Accretion Shocks

This chapter introduces the driving question of this thesis project, "How does magnetic field strength affect accretion shock structure and evolution?", and the strategy to address it with a scaled laboratory-astrophysics experiment. As discussed in Chapter I, a laboratory-astrophysics experiment is considered well scaled when it preserves the dominant physics of the astrophysical system. To ensure this, I developed a six step process, illustrated in Figure 2.1.

1. Qualitatively describe the astrophysical system and define the driving questions of the investigation. These should be questions that the astrophysical community needs answered and, ideally, they should currently elude direct observation and accurate simulation from first principles. See Section 2.1.

2. Qualitatively describe the experiment and define its goals. What flows, objects, and/or fields from Step 1 must be recreated in the lab? Ensure there is a strong visual connection and determine what it is that one intends to measure. See Section 2.2.

3. Research observational studies to determine astrophysical fluid parameters, such as density, temperature, velocity, and so forth. See Section 2.3.

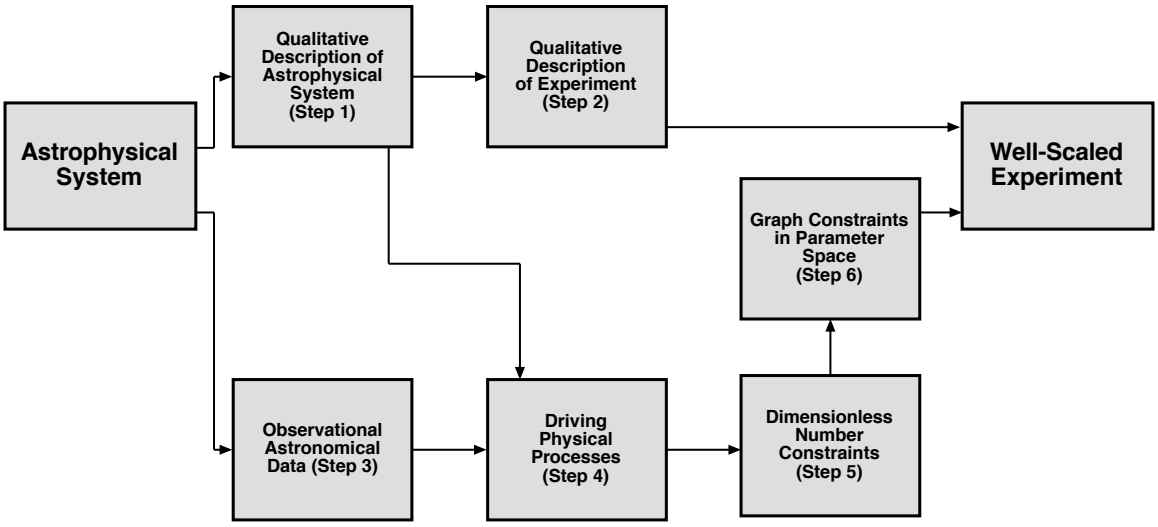

Figure 2.1: The six steps for scaling an astrophysical system to a laboratory experiment.

4. Identify the important physical processes and their associated dimensionless parameters. Because these numbers are dimensionless, they can be used to compare systems on different length scales, such as the astrophysical system and the laboratory experiment. See Section 2.4.

5. Define a list of dimensionless number constraints. These constraints are based on the conditions that exist in the astrophysical system; for the experiment to be well-scaled they must hold true there as well. It is not always necessary to make the dimensionless numbers match exactly, but they should be in similar regimes. See Section 2.5.

6. Map the dimensionless number constraints into the experimental plasma parameter space using region plots that show where the parameter is and is not satisfied. The overlap region where all constraints are satisfied at once defines the parameter range where the experiment will be well-scaled. See Section 2.6.

2.1 Accretion shocks

2.1.1 Evidence for accretion shocks

All stars form at the center of a rotating accretion disks. Our own Sun once passed through this phase of life, and our Solar System is all that remains of the original disk. At that point, the Sun could not sustain hydrogen to helium fusion in its core. Instead it was powered by gravitational contraction and like all young stars, was much more active and variable than it is today. Low mass ($M < 2\mathrm{M}_\odot$) pre-main-sequence stars are called T Tauri stars (*Joy*, 1945; *Herbig*, 1962), while higher mass ones ($2\mathrm{M}_\odot < M < 8\mathrm{M}_\odot$) are called Herbig Ae/Be stars (*Herbig*, 1960), see Table 2.1. (Note: $\mathrm{M}_\odot$ is the solar mass; $\mathrm{R}_\odot$ is the solar radius.)

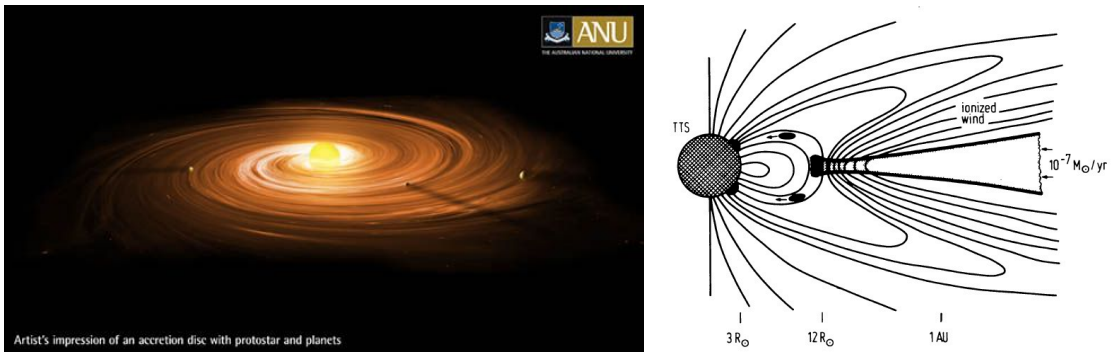

Figure 2.2: Conception of accreting star (left) and diagram of magnetospheric accretion (right).(Image credit: left, Australian National University, and, right, *Camenzind* (1990).)

Parameter	Unit	T Tauri	Herbig Ae/Be
Spectral type	-	K7	A2
Surface temperature, T_*	K	4000	9000
Peak wavelength, λ_{peak}	Å	7200	2900
Stellar mass, M_*	$\mathrm{M}_\odot$	0.8	3.0
Stellar radius, R_*	$\mathrm{R}_\odot$	2.0	3.0
Magnetic field, B	G	2000	100

Table 2.1: Vital statistics for prototypic T Tauri and Herbig Ae/Be stars.

Both T Tauri and Herbig Ae/Be stars are thought to experience magnetospheric

accretion. Originally proposed by *Koenigl* (1991), who extended the compact object work of *Ghosh and Lamb* (1979a,b) to T Tauri stars, the magnetospheric accretion model has material from the accretion disk lifted out of the plane of the disk and "funneled" along the star's magnetic field lines to its surface. (Figure 2.2 depicts a beautiful illustration of this phenomenon.) Today, there is ample evidence that magnetospheric accretion occurs on T Tauri stars (see *Bouvier et al.* (2007) and references therein).

For Herbig Ae/Be stars, the picture is fuzzier. While T Tauri stars have intense magnetic fields of several kiloGauss (*Johns-Krull*, 2007), Herbig Ae/Be stars have magnetic fields of a few hundred Gauss or less (*Hubrig et al.*, 2004, 2006). These magnetic fields are too weak to truncate the star's accretion disk, yet observations suggest that there *are* gaps between Herbig Ae/Be stars and their disks (*Hillenbrand et al.*, 1992; *Dullemond et al.*, 2001; *Natta et al.*, 2001). There is also some evidence of magnetospheric accretion—namely, emission lines that indicate accreting matter is falling rapidly to the stellar surface (*Muzerolle et al.*, 2004; *Natta et al.*, 2000; *Grinin et al.*, 2001).

When the supersonic material impacts the surface of the young star—T Tauri or Herbig Ae/Be—an accretion shock hot enough ($T \sim 10^6 - 10^7\,\mathrm{K}$) to emit soft X-rays forms. There is ample evidence of this in the X-ray spectra of T Tauri stars (*Kastner et al.*, 2002; *Stelzer and Schmitt*, 2004; *Schmitt et al.*, 2005; *Günther et al.*, 2006; *Argiroffi et al.*, 2007; *Robrade and Schmitt*, 2007; *Brickhouse et al.*, 2010; *Argiroffi et al.*, 2011), and evidence is growing that at least some Herbig Ae/Be stars exhibit X-ray-emitting accretion shocks as well (*Swartz et al.*, 2005; *Testa et al.*, 2008; *Grady et al.*, 2010; *Drake et al.*, 2014).

2.1.2 Implications of accretion shocks

The mass accretion rate of a star ($\dot{M}$, usually on the order of $10^{-8}\mathrm{M}_{\odot}$ per year) can be determined from the effect that these X-ray emitting accretion shocks have on the star's spectrum. The X-rays heat the surrounding photosphere, producing spots of hot plasma (*Calvet and Gullbring*, 1998). Compared to a similar non-accreting star, an accreting star ought to have excess emission in the optical and UV due to these spots. From the amount of optical and UV excess, researchers can calculate the fraction of the star's surface covered with accretion streams of a given energy flux (the traditional way to describe accretion streams; $\mathcal{F} = \frac{1}{2}\rho u_s^3$, where u_s is the velocity of the incoming material relative to the shock front), and from there get $\dot{M}$. Using this method, accretion rates for a large population of T Tauri stars are now available (*Hartigan et al.*, 1991; *Valenti et al.*, 1993; *Hartmann et al.*, 1998; *Muzerolle et al.*, 2005; *Natta et al.*, 2006).

In principle, the optical/UV excess method ought to work for Herbig Ae/Be stars as well (the physics is the same), but there is a complication: while T Tauri stars peak in the red or infrared, Herbig Ae/Be stars peak in the blue or UV (see Table 2.1). Discerning their optical or UV excess, therefore, is difficult. Instead, the most common method for measuring Herbig Ae/Be accretion rates depends on the Balmer-γ (Br_{γ}) luminosity (*Garcia Lopez et al.*, 2006; *Mendigutía et al.*, 2011; *Donehew and Brittain*, 2011). However, it should be noted that this method was calibrated using the optical/UV excess method on low and intermediate-mass T Tauri stars (*Muzerolle et al.*, 1998; *Calvet et al.*, 2004).

2.1.3 Open questions regarding structure

These accretion rate calculations are only as good as the understanding of accretion shock structure behind them. Because the surfaces of young stars cannot be spatially resolved, the structure of accretion shocks has not been directly studied.

For example, do accretion shocks penetrate the star's photosphere, potentially hiding much of the accretion shock's energy from observers? Or, do accretion shocks create large "splashes" when they hit the surface of the star, making it appear the shock covers more surface area than it actually does? Either of these scenarios would potentially change the calculated accretion rate significantly.

Brickhouse et al. (2010) addresses this problem head-on for one T Tauri star in particular, TW Hydrae. (Because of its relative closeness and its "pole-on" orientation, TW Hydrae is easily the best studied T Tauri star.) *Brickhouse et al.* estimates that 1.5% of the surface of TW Hydrae is covered with 3-MK plasma, and an additional 6.8% of the surface with 2-MK plasma.

Figure 2.3 illustrates two possible ways to interpret this finding. In Figure 2.3, the cartoons above show a cross section view of accretion shocks hitting stellar surfaces; the one on the left is uncontained and splashes outward violently (see arrows), while the one on the right is contained by the magnetic field (field not shown). The cartoons below correspond to the surface of the star in either scenario. One might have a handful of "splashy," uncontained shocks (see left), or many well-contained shocks (see right). Both cartoon stars have an equal area covered by medium and dark pink, and thus would have the same spectra.

Brickhouse et al. contend that the scenario on the left in Figure 2.3 explains their data: the 3-MK plasma they observed is accretion shocks (dark pink) and the 2-MK plasma they observed is rings (or donuts) of heated stellar atmosphere surrounding the shocks, not additional accretion streams. They note that 3-D simulations by *Romanova et al.* (2004) predict that accretion hotspots should be inhomogenous and irregularly shaped. Similarly, simulations by *Orlando et al.* (2010) found that T Tauri accretion shocks would produce violent outflows, particularly when the magnetic field strength is too low to the contain the accretion shock, see Figure 2.4.

This question is by no means limited to TW Hydrae. In their study of accretion

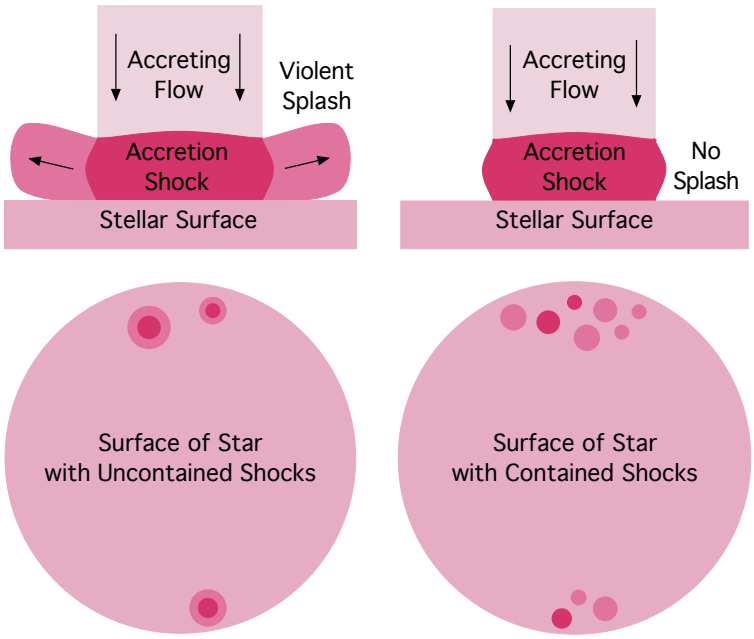

Figure 2.3: Comparison of two different accretion shock scenarios. Are accretion shocks surrounded by violent splashes (left) or are they well-contained (right)?

rates of intermediate-mass T Tauri stars, *Calvet et al.* (2004) write , "Shock models also fail to explain the overall level of the far UV fluxes... An additional source of emission must be contributing in this range, which we still have to identify." They suggest that the emission source might be the pre-shock portion of the accretion column, but the simulations of *Orlando et al.* (2010) suggest that the outflows from accretion shocks might have temperatures and densities similar to those in the pre-shock plasma.

More recently, *Ardila et al.* (2013) published a study of hot gas lines of 28 T Tauri stars and concluded that, "overall, the observations are consistent with the presence of multiple accretion columns with different densities *or* with accretion models that predict a slow-moving, low-density region in the periphery of the accretion column [emphasis added]." Similarly, *Ingleby et al.* (2013) studied 21 T Tauri stars and found that to explain both the UV and the optical excesses, the models required accretion streams ranging from 10^{10} to $10^{12}\,\mathrm{erg\,s^{-1}\,cm^{-2}}$.

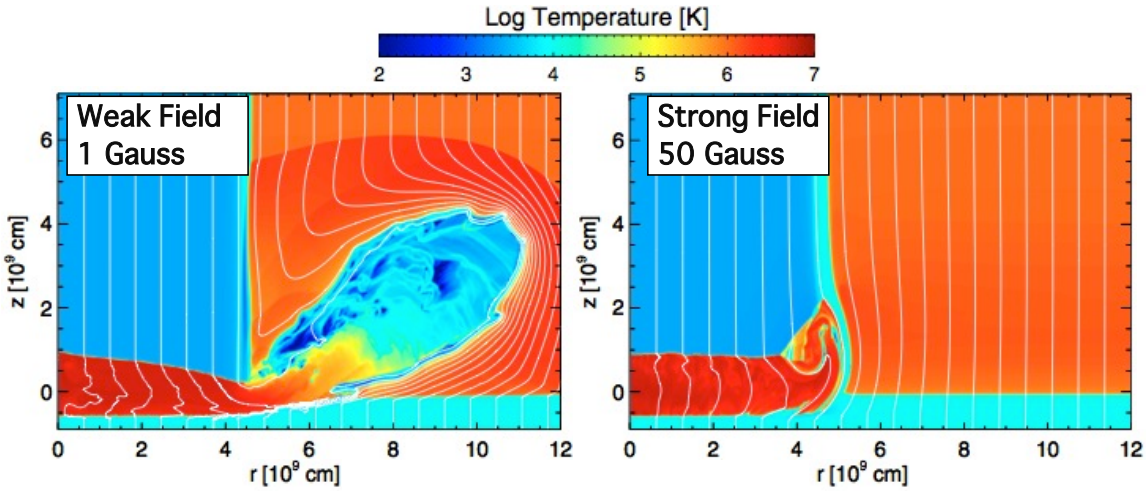

Figure 2.4: Accretion shock simulation results by *Orlando et al.* (2010). The weak field case (left) has a large splash surrounding it, while the strong field case (right) is contained.

This completes Step 1 of the scaling process, "Qualitatively describe the astrophysical system and define the driving questions of the investigation." The system of interest is the region at the surface of the young star when an accretion shock forms and the driving question is how well magnetic fields contain accretion shocks. Ideally, the community needs some way of relating magnetic field strength (which can be directly measured, see Section 2.3) to the degree of containment or the size of the surrounding splash zone.

2.2 Defining the laboratory experiment

Creating an accretion shock motivated experiment requires reproducing the major features of the astrophysical system in the laboratory. Based on the magnetospheric accretion model, accreting flow funnels to the surface of the star along magnetic field lines. It is neither possible nor necessary to reproduce all the aspects of magnetospheric accretion in an experiment. The scope of this experiment is restricted to the area on the stellar surface where the accretion stream impacts to create a shock.

From the frame of reference of an observer on the surface of the star, the stream of accreting material falls (flows down) towards the surface along magnetic field lines that run perpendicular to the stellar surface. (Farther away from the surface of the star, both the streams and the field become more complicated, but this is excluded from the experiment.) Figure 2.5 illustrates the accretion shock system (left) and the laboratory experiment meant to emulate it (right). The experiment requires a plasma jet (the "accreting material") which flows toward a solid block (the "stellar surface") in the presence of a magnetic field running parallel to the jet and perpendicular to the surface (the "stellar field").

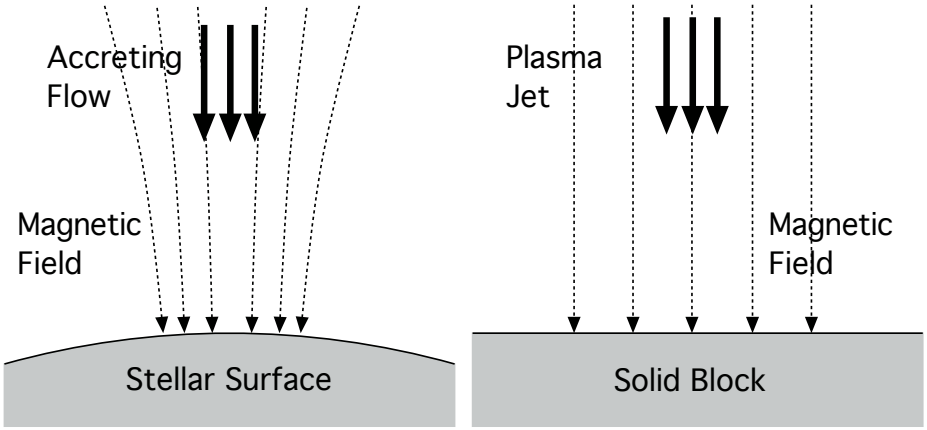

Figure 2.5: Diagram of astrophysical and laboratory accretion shock systems. In the astrophysical system (left), accreting plasma falls to the stellar surface along magnetic field lines (depicted here as a magnetic dipole at the pole of the star). In the lab experiment (right), a plasma jet collides with a solid block with a parallel background magnetic field.

The over-arching goal of the experiment was to determine the connection between magnetic field strength and accretion structure. This was broken down into three subgoals, which are illustrated in Figure 2.6: 1) create an accretion shock in a laboratory experiment (that is a bright/hot/dense region that is distinct from the incoming flow), 2) observe a splash moving out to the sides as time progresses, 3) vary magnetic field to observe a difference in the size and/or outward velocity of the splash.

This completes Step 2 of the scaling process, "Qualitatively describe the exper-

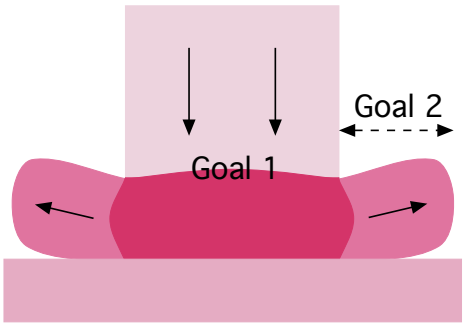

Figure 2.6: Diagram of experimental goals. Goals 1 and 2 are illustrated. Goal 3 was to observe the outflow varying with magnetic field strength.

iment and define its goals." Our experiment required a plasma jet, a solid block to drive it into, and a surrounding magnetic field. The goals were to 1) observe a shock, 2) observe outflows from the shock zone ("splashes") that move with time, and 3) observe a difference in outflow based on magnetic field strength.

2.3 Plasma parameters in accretion shocks

Section 2.1 described the accreting star system on a qualitative level. Understanding the accretion shock in detail requires delving into observational studies of young stars.

X-ray spectra data from T Tauri stars offer important information about accretion shocks, as the X-rays are emitted by the shocked matter. Astronomers typically measure the intensities of many emission lines, anywhere from a dozen to several dozen. The lines are known to be sensitive to the electron density and temperature of the plasma emitting them, so by comparing their relative strengths to a relevant database (generally, the Astrophysical Plasma Emission Database), the astronomers can infer the plasma conditions in the accretion shock. This is not exact science; every spectrum has a range of plasma conditions that could in theory cause it, and that contributes to the error bars astronomers put on their electron density and temperature measurements.

Mass density and incoming velocity can be calculated from incoming velocity as

follows. Mass density is

$$\rho = \frac{Am_p n_e}{Z}, \tag{2.1}$$

where Am_p is the atomic mass, n_e is electron density, and Z is the average ionization. The post-shock temperature is

$$k_B T = \frac{Am_p}{1+Z_2} u_s^2 \frac{2(\gamma_2 - 1)}{(\gamma_2 + 1)^2} \tag{2.2}$$

where u_s is the velocity of the incoming flow *with respect to the shock front*, k_B is the Boltzmann constant, T is temperature, and γ is the adiabatic index. The velocity of the accreting material with respect to the star, u_{acc}, and the velocity of the accreting material with respect to the shock front, u_s, are not the same. (For a complete derivation of this see Section 4.3.3.)

$$u_s = u_{acc} \frac{\gamma - 1}{2}. \tag{2.3}$$

Therefore, incoming velocity of the accreting material with respect to the star can be calculated as,

$$u_{acc} = \left[\frac{2(1+Z)k_B T}{(\gamma - 1)Am_p} \right]^{1/2}, \tag{2.4}$$

assuming that the average atomic number and average mass number in the accretion shock are assumed to be that of the sun: $Z_* = 1.1$ and $A_* = 1.3$. Table 2.2 presents the findings of eight T Tauri spectral studies and calculated values for mass density, ρ, and incoming velocity, u_{acc}.

The velocity values in Table 2.2 are calculated from shock temperature, but in-fall velocities can also be directly measured from Doppler shifts or calculated from the free-fall velocity formula. *Edwards et al.* (1994) found that absorption lines in T Tauri

Paper	Subject	T[MK]	$\log[n_e\ \mathrm{cm}^{-3}]$	$\log[\rho\,\mathrm{g\,cm}^{-3}]$	$u_{acc}[\,\mathrm{km\,s}^{-1}]$
Kastner et al. (2002)	TW Hya	3	13	-10.7	400
Stelzer and Schmitt (2004)	TW Hya	3	13	-10.7	400
Schmitt et al. (2005)	BP Tau	2.5	11.5	-12.2	370
Günther et al. (2006)	V4046 Sag	3	11.8	-11.9	400
Argiroffi et al. (2007)	MP Mus	3	11.7	-12.3	400
Robrade and Schmitt (2007)	RU Lup	2.8	11.5	-12.2	390
Brickhouse et al. (2010)	TW Hya	2.5	12.5	-10.7	370
Argiroffi et al. (2011)	V2129 Oph	3.5	12.1	-11.6	430

Table 2.2: Plasma conditions in accretion shocks, based on X-ray spectral analysis of T Tauri stars.

spectra were redshifted 200 to 300 $\mathrm{km\,s}^{-1}$. The free-fall formula is

$$u_{\mathrm{ff}} = \sqrt{\frac{2GM}{R_f}\left(1 - \frac{R_f}{R_i}\right)}, \tag{2.5}$$

where G is the gravitational constant, M is the mass of the star, R_f is the final radius, and R_i is the initial radius. For typical T Tauri values of $R_* = 2\mathrm{R}_\odot$ and $M_* = 0.8\mathrm{M}_\odot$ (see Table 2.1), and assuming $R_i = 5R_8$, $u_{\mathrm{ff}} = 350\,\mathrm{km\,s}^{-1}$, so this is consistent.

Accretion shock studies quantify accretion stream strengths in terms of energy flux, $\mathcal{F} = \frac{1}{2}\rho_1 u_1^3$, where ρ_1 and u_1 are the density and velocity upstream of the accretion shock. Calculated values of $\mathcal{F}$ range from 10^{10} to $10^{12}\,\mathrm{erg\,s}^{-1}\,\mathrm{cm}^{-3}$ (*Ingleby et al.*, 2013). If incoming velocities range from 200 to 400 $\mathrm{km\,s}^{-1}$, this corresponds to $\rho_1 \approx 10^{-13}$–$10^{-10}\,\mathrm{g\,cm}^{-3}$, which is consistent with the post-shock density values found in Table 2.2.

Pre-shock temperature is difficult to observe directly, but can be estimated. *Calvet and Gullbring* (1998) used a numerical simulation to determine the temperature of the pre-shock region and found that it was 15,000–25,000 K, due to preheating from X-ray emission from the accretion shock itself. Meanwhile, the background temperature of a T Tauri star puts the lower limit of the incoming temperature at around 4000 K.

The last parameter is magnetic field strength, which can be determined from

Zeeman broadening. The Zeeman effect is a single spectral line splitting due to the presence of a magnetic field; in this application the split lines blur together. *Johns-Krull et al.* (1999) measured Zeeman broadening in the infra-red spectrum of BP Tau to determine that its field is 2.6 kG. *Valenti and Johns-Krull* (2004) applied the same technique to seventeen T Tauri stars and found magnetic field strengths from 1 to 3 kG. This is consistent with later findings by *Yang et al.* (2005) and *Johns-Krull* (2007).

Wade et al. (2007) studied circularly polarized light from a wide sample of Herbig Ae/Be stars and found that most do not have a measurable field, although a handful have fields on par with T Tauri stars (a kG or more). In general, Herbig Ae/Be stars have fields of a few hundred G, if they have any at all.

Table 2.3 summarizes the findings of this section and completes Step 3, "Research observational studies to determine astrophysical plasma parameters."

Parameter	Unit	Range
Incoming velocity, u	$\mathrm{km\,s^{-1}}$	200–400
Incoming energy flux, $\mathcal{F}$	$\mathrm{erg\,s^{-1}\,cm^{-2}}$	10^{10}–10^{12}
Incoming mass density, ρ	$\mathrm{g\,cm^{-3}}$	10^{-13}–10^{-10}
Incoming temperature, T	K	4000–25000
Magnetic field, B	G	0–3000

Table 2.3: Plasma parameter ranges for accretion shocks

2.4 Physical processes and dimensionless numbers

Astrophysical systems can never be scaled and reproduced perfectly in the lab. Having a worthwhile experiment, therefore, hinges on discerning which physical processes are most important and translating them into an experiment appropriately. *Ryutov et al.* (1999) lays out a theoretical basis for doing so: one must ensure that dimensionless numbers (for example, Reynolds number) that define the system are at least in similar regimes.

To review from Section 2.2, our goals are 1) create an accretion shock in a laboratory experiment (that is a bright/hot/dense region that is distinct from the incoming flow), 2) observe a splash moving out to the sides as time progresses, 3) vary magnetic field to observe a difference in the size and/or outward velocity of the splash.

Accomplishing this requires, first and foremost, that plasma conditions allow a shock to form in the first place. This requires a supersonic flow (see Section 2.4.1) and, because the shock will form on the length scale of the ion-ion mean free path (MFP), a relatively short MFP (see Section 2.4.2). In order to observe the effects of a magnetic field, the magnetic diffusion length must be short enough to allow the field to persist during the experiment (see Section 2.4.3). The ram plasma β (see Section 2.4.4) is the ratio of field strength pressure to material pressure. Translating this accurately into the lab is crucial to understanding the connection between field strength and shock containment. Finally the Reynolds numbers must be in the same rough regime (see Section 2.4.5).

2.4.1 Mach number

$\mathcal{M}$ is the Mach number, the ratio of the flow velocity of the jet to the speed of sound inside the jet, $\mathcal{M} = u/c_s$. Sound speed was calculated according to

$$c_s = 9.79 \times 10^5 \sqrt{\frac{\gamma(Z+1)T_e}{A}}\,\mathrm{cm\,s^{-1}}, \tag{2.6}$$

where γ is the adiabatic index, Z is the average ionization, T_e is the temperature in eV, and A is the atomic mass in proton masses.

2.4.2 Mean free path

λ_{MFP} is the ion-ion mean free path inside the plasma. Any mean free path can be expressed as $\lambda = 1/(n\sigma)$, where n is the number density and σ is the cross-section.

The ion-ion mean free path is

$$\lambda_{\mathrm{MFP}} = \frac{1}{n_i \sigma_{90}^{ii} 4 \ln \Lambda_{ii}}, \tag{2.7}$$

where n_i is the ion density and $\sigma_{90}^{ii} 4 \ln \Lambda_{ii}$ is the total cross section expressed as the 90° cross-section, σ_{90}^{ii}, with a correction factor of $4 \ln \Lambda_{ii}$ to account for collisions between ions that fail to deflect an ion a full 90°. The 90° cross-section was calculated according to

$$\sigma_{90}^{ii} = \frac{\pi e^4 Z^4}{m_i u^4}, \tag{2.8}$$

where e is the charge of an electron, Z is the average ionization, m_i is the ion mass, and u is the relevant velocity (in this case the flow velocity).

2.4.3 Magnetic diffusion length

ℓ_M is the magnetic diffusion length scale. Any diffusion length scale can be written as ν/u, where ν is the diffusion coefficient and u is the relevant velocity. Here we are concerned with magnetic diffusion in the post-shock region, so the diffusion coefficient is ν_M and the velocity is $u_2 = u_1/4$, where u_1 is pre-shock velocity and u_2 is post-shock velocity, taking the strong shock limit of the Rankine-Hugoniot shock conditions. Therefore we have

$$\ell_M = \frac{\nu_M}{u_2} = \frac{4\nu_M}{u_1}, \tag{2.9}$$

The magnetic diffusivity in Gaussian CGS units is

$$\nu_M = \frac{c^2 \eta_\perp}{4\pi}, \tag{2.10}$$

where $\eta_\perp$ is the transverse Spitzer resistivity, yielding

$$\ell_M = \frac{c^2 \eta_\perp}{\pi u_1}. \tag{2.11}$$

The expression for transverse Spitzer resistivity is taken from the *Plasma Formulary*, (*Huba et al.*, 2009):

$$\eta_{\perp} = 1.15 \times 10^{-14} \frac{Z \ln \Lambda}{T_e^{3/2}} \text{ sec}, \tag{2.12}$$

where Z is the ionization, $\ln \Lambda$ is the Coulomb logarithm, and T_e is the electron temperature in eV.

2.4.4 Ram plasma β

β_{ram} is the ratio of ram pressure of the jet to the magnetic pressure of the field

$$\beta_{\text{ram}} = \frac{\rho u^2}{B^2/8\pi}, \tag{2.13}$$

where B is magnetic field strength.

2.4.5 Viscosity and Reynolds number

Re is the Reynolds number, the ratio of the viscous timescale to the dynamic timescale, $Re = Lu/\nu$, where L is the relevant length scale, u is the relevant velocity, and ν is the ion-ion viscosity, which was calculated according to

$$\nu_i = \frac{u_{th,i}^2}{\nu_{ii}} = 2 \times 10^{19} \frac{T_i^{5/2}}{n_i Z^4 \sqrt{A} \ln \Lambda} \text{ cm}^2 \text{ s}^{-1}, \tag{2.14}$$

where $u_{th,i}$ and ν_{ii} are the ion thermal velocity and the ion-ion collisional frequency, respectively, and expressions for both were taken from the *Plasma Formulary*, (*Huba et al.*, 2009). In the expression for ν_i, T_i is the ion temperature in eV, n_i is the ion density in cm^{-3}, Z is the ionization, A is the atomic mass, and $\ln \Lambda$ is the Coulomb logarithm.

This completes Step 4 of the scaling process, "Identify the important physical process and their associated dimensionless numbers." The five dimensionless numbers

of interest are Mach number, ion-ion mean free path, magnetic diffusion length scale, ram plasma beta, and Reynolds number.

2.5 Constraints for the experiment

Section 2.4 laid out five dimensionless numbers that capture the relevant physics of the accretion shock: Mach number, ion-ion mean free path, magnetic diffusion length scale, ram plasma beta, and Reynolds number. Table 2.3 listed the ranges of plasma parameters that one might expect in accretion shocks. Figure 2.7 shows the five dimensionless numbers from Section 2.4 plotted over the range of inputs typical of accreting star systems.

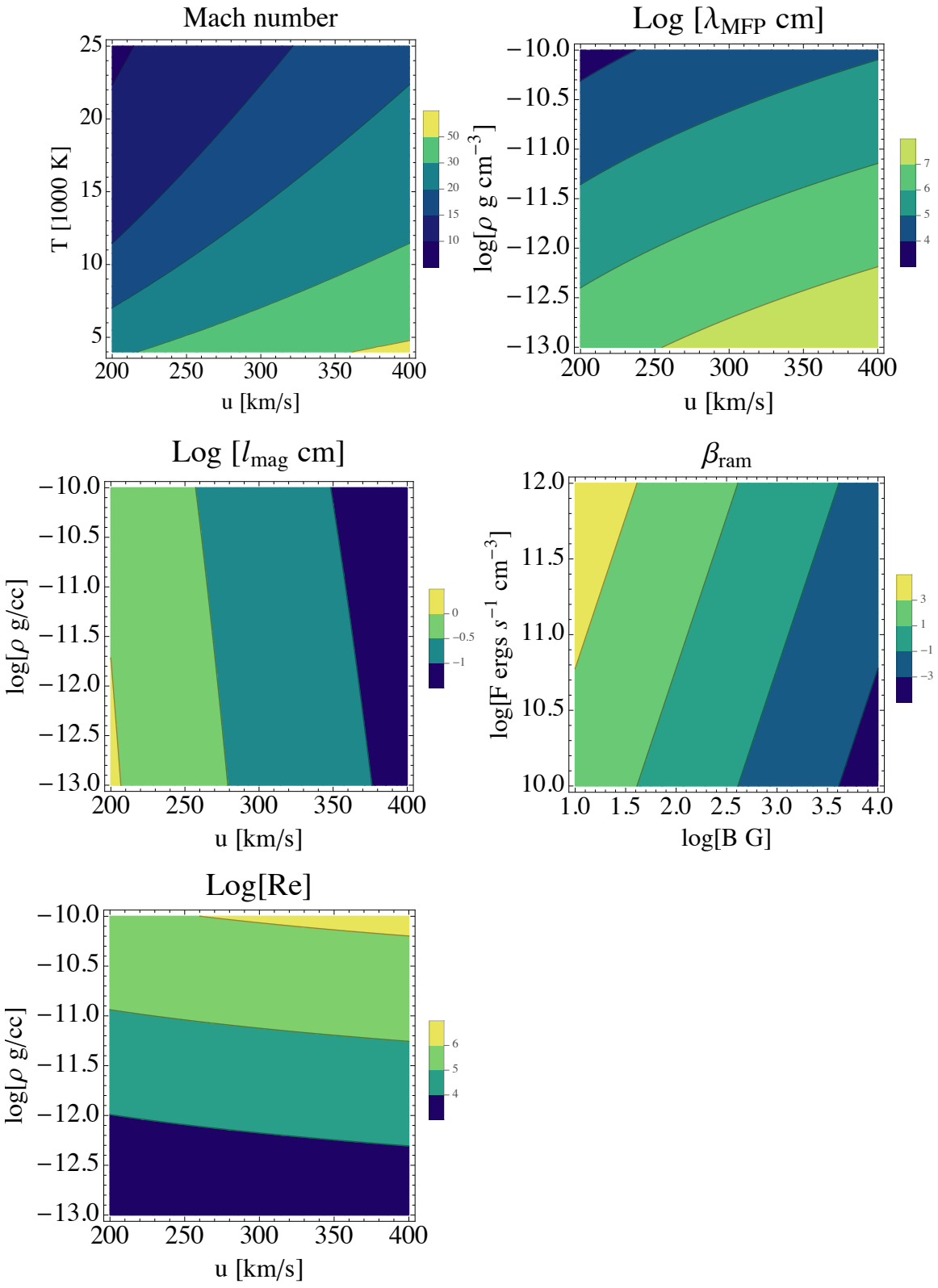

Figure 2.7: Density-velocity space plots of dimensionless numbers in astrophysical accretion shocks. Plots of ion-ion MFP, Mach number, magnetic diffusion length, ram plasma β, and Reynolds number for accretion shock conditions.

We can draw the following conclusions from Figure 2.7:

1. The flow is highly supersonic. Over the range of velocities and temperatures possible for the incoming flow, Mach numbers ranging from 5 to 50. This is expected as accretion shock appear to be common on actively accreting stars. We can translate this into the lab by imposing $\boldsymbol{\mathcal{M} > 1}$.

2. Ion-ion MFP is much less than the length scale of the system over the whole range of inputs. For the ranges of incoming velocity and incoming density possible, the ion-ion MFP ranges from 10^4–10^8 cm; the length scale of the astrophysical system is 10^9 cm. We can translate this into the lab by imposing $\boldsymbol{\lambda_{\mathrm{MFP}} < L}$.

3. Magnetic diffusion length is much less than the length scale of the system. For the ranges of incoming velocity and incoming density possible, the magnetic diffusion length is 0.1–1 cm. We can translate this into the lab by imposing $\boldsymbol{\ell_M < L}$.

4. Ram plasma beta, β_{ram} is plotted for magnetic field strength and incoming material energy flux, which was defined in Section 2.3. Over the ranges of field strengths and energy fluxes possible, $\beta_{\mathrm{ram}} = 10^{-3}$–$10^3$. That covers three regimes: $\beta_{\mathrm{ram}} \gg 1$, $\beta_{\mathrm{ram}} \approx 1$, and $\beta_{\mathrm{ram}} \ll 1$. The high beta case is easy to achieve; one can always run a control with a low field. Therefore the scaling arguments presented in this thesis are for $\beta_{\mathrm{ram}} \approx 1$ and this was done by imposing $\boldsymbol{0.1 < \beta_{ram} < 10}$.

5. Reynolds numbers are much greater than a thousand across the input range. We can translate this into the lab by imposing $\mathbf{Re > 10^3}$.

This completes Step 5, "Define a list of dimensionless number constraints." The constraints that will be imposed on the laboratory experiment are listed in bold above.

2.6 Mapping the constraints to parameter space

To be well-scaled, the experiment must have the five criteria listed at the end of Section 2.5 be true at once. For every material, there is some four-dimensional volume in T_e–u–ρ–B space where all five of these criteria are simultaneously met.

A four dimensional space is difficult to visualize, much less translate into a figure. In order to investigate the parameter space, I held T_e and B constant and considered the 2-D u–ρ space; this is illustrated in Figures 2.8 and 2.9. In each of the plots in these figures, the shaded area represents the region in u–ρ space where the criterion is not met. Obviously, this area will shift depending on material type, temperature and magnetic field strength. Figures 2.8 and 2.9 give two temperature options for a CH (plastic) plasma in a 10-T magnetic field. Plastic is a commonly used material for target fabrication; it seemed a reasonable assumption for an experimental plasma. MIFEDS can impose magnetic fields in the range of 5–15 T *Fiksel et al.* (2015); but from the perspective of scaling, there is no disadvantage to having a high magnetic field.

Considering Figures 2.8 and 2.9, one can see what conditions each criterion favors and whether high or low temperatures are more limiting. Along the left hand side of the plots, the first criterion, Mach number, and the third criterion, magnetic diffusion length, rule out very low-velocity flows. Both favor high velocity because $\mathcal{M} \propto u$ and $\ell_M \propto 1/u$. At low temperatures, ℓ_M is more limiting. As the temperature rises, Mach number becomes more limiting as sound speed rise and ℓ_M drops according to $\ell_M \propto 1/T^{3/2}$.

Along the bottom of the plots, the second criterion, ion-ion mean free path, and the fifth criterion, Reynolds number, rule out low-density flows. The mean-free-path constraint favors high density, low velocity conditions, because $\lambda_{\mathrm{MFP}} \propto 1/n_i$ and $\lambda_{\mathrm{MFP}} \propto u^4$. Reynolds number favors high velocity, high density conditions because $Re \propto u$ and $\nu_i \propto n_i$. At low temperatures, mean free path is more limiting, while

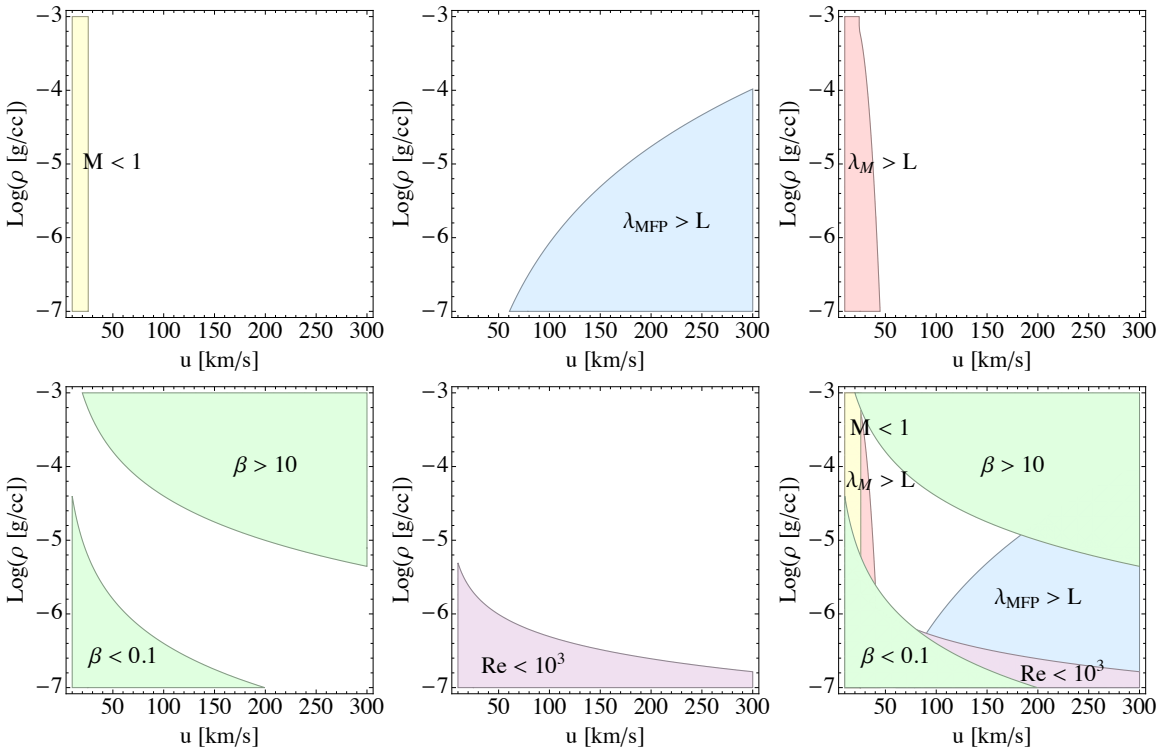

Figure 2.8: Criteria region plots for a CH experiment at 10 eV with a 10 T field. Each region plot delineates the region where the condition is met (blank) and the region where it is *not* met (colored). Top row: Mach number, mean free path, and magnetic diffusion length. Bottom row: ram plasma β, Reynolds number, and all criteria plotted at once.

at high temperatures Reynolds number is more limiting. The mean-free-path trend is due to ionization. Higher ionization raises the collisional cross-section of the ions; larger cross section means more collisions. The Reynolds number trend is due to ionization and the direct effects of temperature itself; the ion viscosity is thermal velocity squared over ion-ion collisional frequency. Although ion-ion collisional frequency increases with increasing temperature, the thermal velocity dependence wins out and increasing temperature increases the viscosity, thus decreasing the Reynolds number.

Finally, the fourth criterion, ram plasma β, rules out both low-density, low-velocity flows due to the $\beta_{\text{ram}} > 0.1$ constraint, and high-velocity, high-density flows due to

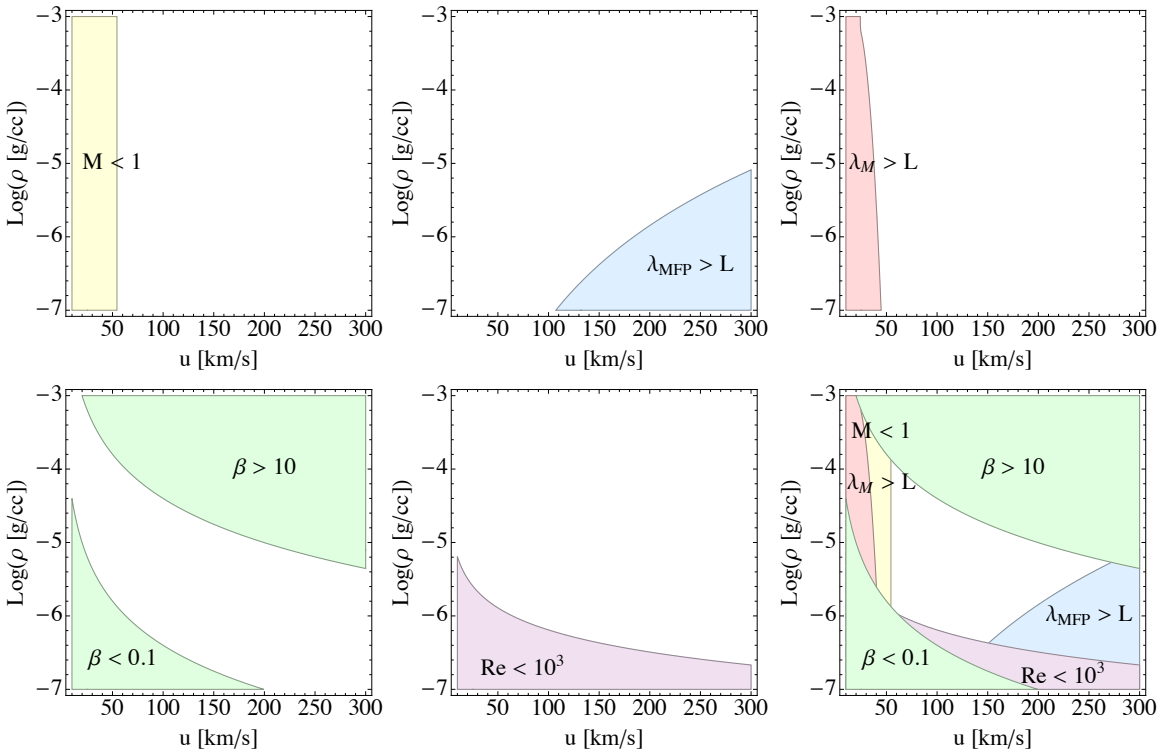

Figure 2.9: Criteria region plots for a CH experiment at 30 eV with a 10 T field. Layout and color-coding are the same as Figure 2.8.

the $\beta_{\text{ram}} < 10$ constraint. Of the two, the $\beta_{\text{ram}} < 10$ constraint is more limiting; in practice low-density, low-velocity flows are difficult to achieve on a laser. Because β_{ram} has no temperature dependence, it does not change between Figures 2.8 and 2.9.

Taking all five constraints together, a 10-eV CH plasma, see Figure 2.8, would require $\rho \sim 10^{-5}\,\text{g}\,\text{cm}^{-3}$ and $u \sim 100\,\text{km}\,\text{s}^{-1}$, while a 30-eV CH plasma, see Figure 2.9, would require $\rho \sim 3 \times 10^{-6}\,\text{g}\,\text{cm}^{-3}$ and $u \sim 150\,\text{km}\,\text{s}^{-1}$.

Table 2.4 presents the plasma parameters and calculated length scales and dimensionless numbers for the astrophysical system and both experimental plasma options.

This completes Step 6, "Map the constraints into parameter space and find the volume where all of them are satisfied." When the highest plausible magnetic field on OMEGA, 10 T, is imposed, the constraints are satisfied for a 10-eV CH plasma with $\rho \sim 10^{-5}\,\text{g}\,\text{cm}^{-3}$ and $u \sim 100\,\text{km}\,\text{s}^{-1}$, or a 30-eV CH plasma with $\rho \sim 3 \times 10^{-6}\,\text{g}\,\text{cm}^{-3}$

Parameter	Unit	Accreting Star	10 eV Experiment	30 eV Experiment
Mass density, ρ	$\mathrm{g\,cm^{-3}}$	2×10^{-11}	10^{-5}	3×10^{-6}
Average atomic number	-	1.1	6.5	6.5
Average mass number	-	1.3	3.5	3.5
Average ionization	-	0.7	2.4	3.5
Electron density, n_e	$\mathrm{cm^{-3}}$	7×10^{12}	2×10^{18}	10^{18}
Electron temperature, T_e	eV	1	10	30
Velocity, u	$\mathrm{km\,s^{-1}}$	450	100	150
Magnetic field strength, B	G	1000	10^5	10^5
Post-shock temperature, T_s	eV	300	40	80
Length scale, L	cm	10^9	0.1	0.1
Ion collisional MFP, $\lambda_{\mathrm{MFP,i}}$	cm	2×10^6	0.02	0.03
Magnetic diffusion length, ℓ_M	cm	200	0.03	0.01
Mach number, $\mathcal{M}$	-	30	4	3
Collisionality, $\lambda_{\mathrm{MFP,i}}/L$	-	0.002	0.2	0.3
Magnetic diffusion length ratio, λ_M/L	-	2×10^{-7}	0.3	0.1
Ram Plasma Beta, β_{ram}	-	1.0	2.5	1.7
Reynolds number, Re	-	10^{10}	3×10^4	10^4

Table 2.4: Comparing typical numbers in an accretion stream to two options for experimental jets.

and $u \sim 150\,\mathrm{km\,s^{-1}}$. If the incoming plasma jet has parameters in either of these ranges, or something in between, an experiment resembling Figure 2.5 will be well-scaled.

CHAPTER III

Collimated Jet Experiments

Chapter II related the process for scaling an astrophysical accretion shock to the laboratory and ended with two sets of plasma parameters, either of which would yield a well-scaled accretion shock experiment.

In April 2012, our collaboration dedicated a day of experiments on OMEGA to testing a method for creating collimated jets with plasma parameters similar to those determined in Chapter II.[1] We conceived of a simple experiment: we would irradiate the rear side of thin cones of acrylic to launch collimated plasma jets and characterize them with optical Thomson scattering and 2-D visible light imaging. This chapter discusses those experiments, the results we obtained, and my analysis of the jet structure.

Section 3.1 discusses the motivation for developing collimated plasma jets and related jet work by other researchers. Section 3.2 delves into my analytical theory of how a conical target collimates the jet. Section 3.3 presents the experimental set-up, experimental parameters used, and discusses what data were obtained.

Section 3.5 presents the Thomson data and its analysis. Thomson scattering is a method for ascertaining parameters such as temperature and density of an experimental plasma by scattering a laser beam of known wavelength off the experimental

[1] Chronologically, this work was completed *before* the accretion shock experiment was undertaken, but even in April 2012 our collaboration anticipated needing steady, collimated jets for more complex future experiments.

plasma and analyzing the scattered spectrum. We obtained density, temperature and velocity data from seven shots, two colliding jet and five single jet.

Section 3.4 presents the 2-D visible light images obtained; these self-emission images clearly show the jets, their collimation, and how they evolve when collided with each other.

Section 3.6 presents my conclusions.

3.1 Previous Work

Collimated plasma jets are an essential building block in more complicated experiments. One commonly used technique for creating a collimated jet is irradiating either side of a conical or V-shaped target. While plasma from a flat target will expand in all directions without encountering any opposing flow, plasma from a V-shaped or conical target will collide with the plasma flowing away from the opposite side of the target, creating a collimated plasma jet, see Figure 3.1.

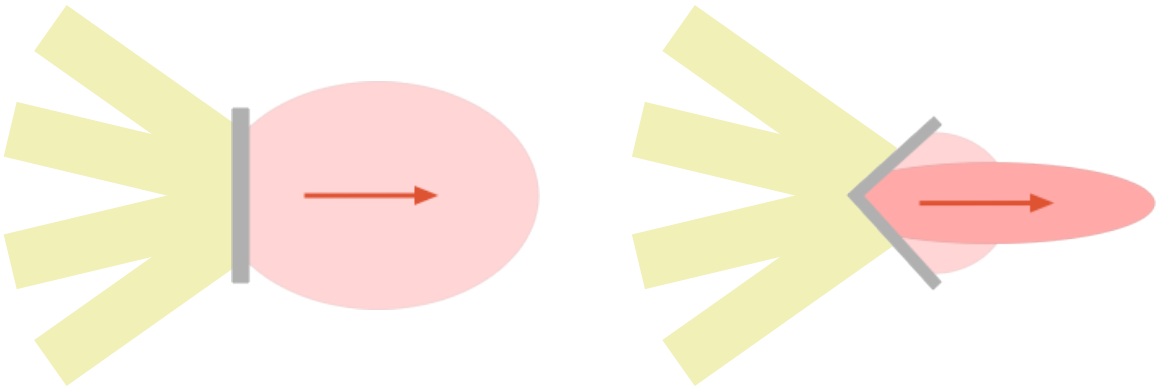

Figure 3.1: Plasma flows from flat vs. V-shaped or conical targets. Unlike a plasma front emanating from a flat target (top), a V-shaped or conical target, produces a collimated plasma jet (bottom). The yellow represents the laser beams irradiating the rear side of the target, the gray represents the target (seen here in cross-section), and the pink represents the plasma created.

When a laser pulse hits a thin target, it immediately releases plasma on the

irradiated surface and drives a shock wave into the target. The shock wave heats the material as it passes through, vaporizing it and creating a hot, dense reservoir of plasma that expands in both directions. The surface the laser hit is known as the front surface; the opposite surface is known as the rear surface. The flow from the front surface is the hot, fast initial release followed by the slower, denser expanding rarefaction. However, when this surface is used to create jets (known as "front-surface" jets) is it usually the hot, fast initial flow that is of interest. Thus front-surface jets are typically hotter and faster than rear-surface jets. Table 3.1 presents the results of four other teams that used V-shaped or conical targets. One team, *Li et al.* (2013), had yet to publish when these experiments were designed, but is included here because it represents a medium-Z material.

Parameter	Unit	Farley	Shigemori	Gregory	Li
Irradiated surface	-	Front	Front	Rear	Front
Material	-	Au	Al	Al	CH
Mass density, ρ	$\mathrm{g\,cm^{-3}}$	0.05	10^{-3}	10^{-4}	10^{-4}
Electron temperature, T_e	eV	250	200	10	750
Velocity, v	$\mathrm{km\,s^{-1}}$	500	700	300	1700

Table 3.1: Results of V-shaped or conical experiments. Studies cited are *Farley et al.* (1999); *Shigemori et al.* (2000); *Gregory et al.* (2008); *Li et al.* (2013).

3.2 Theory

This section presents analytical calculations for the shape of the collimated jet that were done prior to the April 2012 experiment. The underlying assumption is that a stagnation shock forms. Outside the stagnation shock, the plasma flows perpendicular to the original surface of the target (that is, towards the axis of the cone); inside the shock, the radial flow is stagnated and the flow is entirely in the axial direction.

As illustrated in Figure 3.2, when the flow encounters the shock front, described by $r(z)$, its direction bends to be parallel to the axis. Locally, the incoming flow

approaches an oblique shock with some angle ϕ_1 with respect to the surface normal, $\hat{n}$, and leaves the shock with angle ϕ_2 with respect to $\hat{n}$. Some basic geometry yields $\phi_1 = \theta - \alpha$ and $\phi_2 = 90° - \alpha$, where α is the local angle between the z-axis and the shock profile and θ is the opening half-angle of the cone.

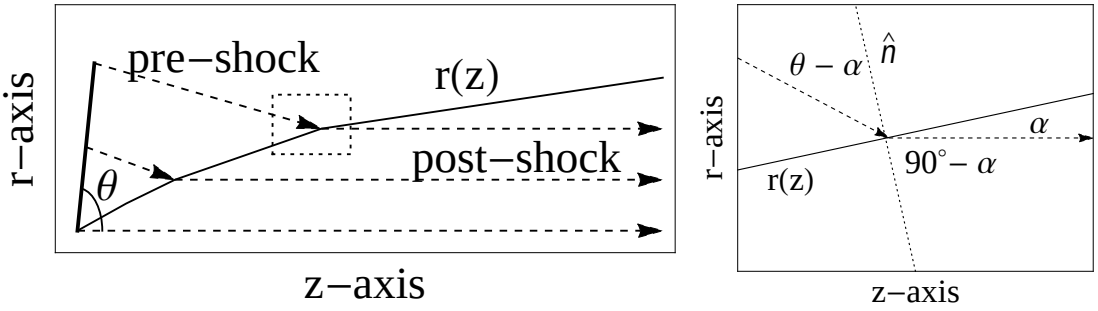

Figure 3.2: Collimating shock profile diagram. When plasma encounters the shock profile, described by $r(z)$, it bends to become parallel to the z-axis. The diagram on the right is a zoomed-in view of the dotted line box in the diagram on the left.

From equation 4.33 of *Drake* (2006), the flow at the oblique shock front will bend according to,

$$\cot\alpha = \tan(\theta - \alpha)\frac{\mathcal{M}_n^2(\gamma+1)}{\mathcal{M}_n^2(\gamma-1)+2}, \tag{3.1}$$

where $\mathcal{M}_n$ is the normal upstream Mach number, $\mathcal{M}_n = \mathcal{M}\cos(\theta - \alpha)$.

Solutions to Equation 3.1 are illustrated in Figure 3.3 for $\theta = 80°$ and $\gamma = 1.5$. At low Mach numbers, there are no solutions to Equation 3.1. Physically, this is due to the assumption that $u_r = 0$ in the post-shock region; the shock is not strong enough to "bend" the flow all the way to the direction of the z-axis and the assumptions behind Equation 3.1 no longer hold. At some critical Mach number, $\mathcal{M}_c$, there is exactly one solution and for $\mathcal{M} > \mathcal{M}_c$ there are two solutions. Of these two solutions, the lower branch is physical; a higher Mach number will produce a tighter jet. As $\mathcal{M} \to \infty$, $cot\alpha = \tan(\theta-\alpha)(\gamma+1)/(\gamma-1)$, which has the solution 2.5° for $\gamma = 1.5$ and $\theta = 80°$.

There is one final assumption for this problem: the flow coming off the surface of the target (or more accurately, where the target was prior to the laser pulse) can be

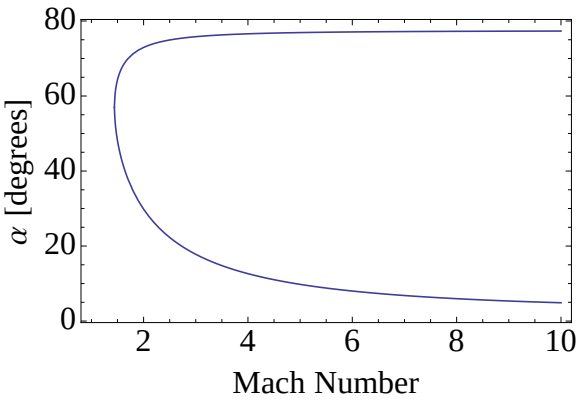

Figure 3.3: Bending angle vs. Mach number. For any Mach number over $\mathcal{M}_c$, there are two values of α that satisfy Equation 3.1.

described as a drifting rarefaction, that is, $u = u_{\text{rare}} + u_{\text{drift}}$, where u is the velocity, u_{rare} is the velocity in the frame of reference of the plasma reservoir, and u_{drift} is a drift velocity. u_{drift} accounts for the added momentum the laser pulse imparts to the system; it is the velocity of the plasma reservoir with respect to the lab.

I found $r(z)$ using an iterative scheme in *Mathematica*:

1. Assume some shock profile, $r_i(z)$. This could in principle be any profile, but for simplicity I used a straight line with an opening half-angle of $\theta/2$.

2. For every point along $r_i(z)$, calculate its distance from the target wall, $x_i(z)$. Calculate the Mach number, $\mathcal{M}_i(z)$, based on analytic models of rarefactions.

3. Having $\mathcal{M}_i(z)$, calculate the bending angle along the shock profile, $\alpha_i(z)$.

4. Use $\alpha_i(z)$ to construct a more refined shock profile, $r_{i+1}(z)$.

5. Repeat Steps 1–4 until $r_n(z)$ converges.

The Mach number will be a function of distance from the original target surface and time. For an isothermal rarefaction with a drift velocity, u_d, Mach number is

$$\mathcal{M}_{\text{iso}}(x,t) = 1 + \frac{x}{c_s t} + \frac{u_d}{c_s}, \tag{3.2}$$

where c_s is the speed of sound. For an adiabatic rarefaction with a drift velocity, u_d, Mach number is

$$\mathcal{M}_{\mathrm{ad}}(x,t) = \frac{\frac{2}{\gamma+1}\left(c_o + \frac{x}{t}\right) + u_d}{c_o - \frac{\gamma-1}{2}\frac{x}{t}} \tag{3.3}$$

where c_o is the speed of sound in the original reservoir. Figure 3.4 compares shock profiles, $r(z)$, created by comparable adiabatic and isothermal rarefactions. Because the adiabatic rarefaction cools as it expands, it has higher Mach numbers and creates a more collimated jet.

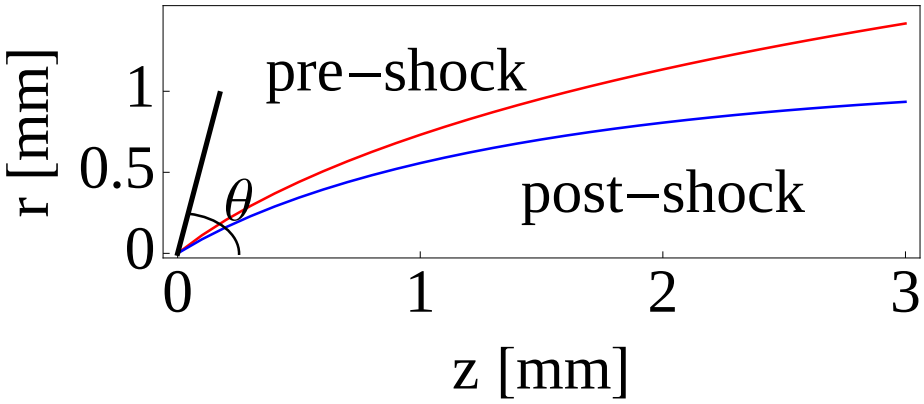

Figure 3.4: Calculated collimating shock profiles for adiabatic and isothermal rarefactions. Blue represents the shock profile created by an adiabatic rarefaction with $t = 30\,\mathrm{ns}$, $c_o = 40\,\mathrm{km\,s^{-1}}$, and $u_d = 20\,\mathrm{km\,s^{-1}}$. Red represents the shock profile created by an isothermal rarefaction with $t = 30\,\mathrm{ns}$, $c_s = 40\,\mathrm{km\,s^{-1}}$, and $u_d = 20\,\mathrm{km\,s^{-1}}$.

This analysis rests on several simplifying assumptions: that the flow off the sides of the target was a perfect rarefaction (isothermal or adiabatic), that the reservoir of plasma that launched the rarefaction never ran out, and that the flow stagnated completely inside the shock structure. The reality will inevitably be more complicated, but the analysis of this chapter underscores the validity of using conical targets to create a collimated jet.

3.3 Experiment

In April 2012, our experimental team devoted a day of shots to launching jets by irradiating thin cones similar to those sketched in Figure 3.1. We chose to use Poly(methyl methacrylate) or PMMA ($C_5H_8O_2$), hereafter referred to simply as acrylic, to create the jets. Acrylic is a moderate Z-number material that is non-toxic and lends itself to micro-machining. Using acrylic allowed us to have the targets machined in-house at the University of Michigan, which provided flexibility during the shot planning process.

As discussed in Section 3.1, if a thin target is irradiated, the resulting rarefaction from either the front or the rear side may be used. Front-side jets tend to be hotter, faster and shorter-lived, while rear-side jets are colder, slower and longer-lived. We chose rear-side irradiation because we anticipated needing long-lived jets for experiments lasting 10's of nanoseconds. The experimental scheme is seen in Figure 3.5. Two cones 6 mm apart, and each 3 mm from target chamber center, were rear-irradiated, launching collimated jets. These jets could each be launched individually or they could be launched together to form a head-on collision; all three possibilities were shot multiple times.

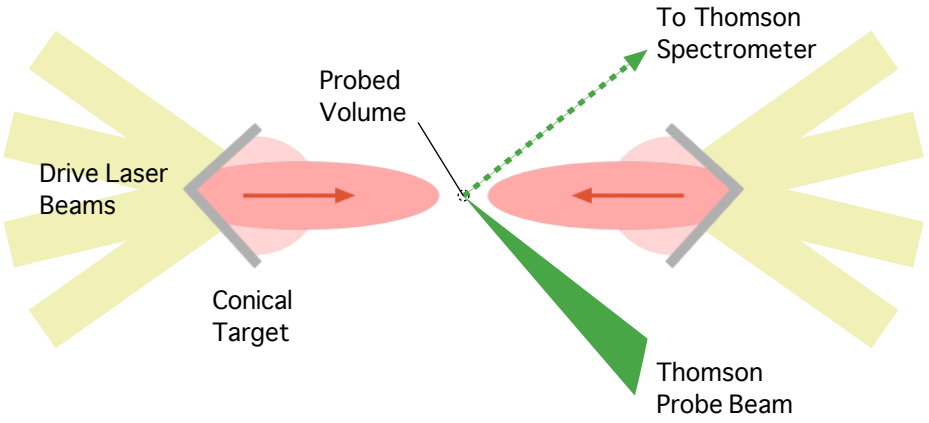

Figure 3.5: Experimental configuration from April 2012.

The primary diagnostic used was 2ω (526.5 nm) Thomson scattering aimed at the

mid-point of the experiment (3 mm from each jet launch point). Thomson scattering is a technique for measuring plasma parameters such as density and temperature by scattering a probe laser beam at the experimental plasma and collecting and analyzing the scattered spectrum. As a secondary diagnostic, we recorded self-emission images of our jets with a 2-D visible light imager. The imager was gated to 3 ns (the shortest possible gating time) and filtered with a 3ω long pass filter, which blocks wavelengths shorter than 385 nm, and a 1.0 neutral density filter. Both of these diagnostics are discussed in detail in Appendix A.

Table B.1 lists the experimental parameters for the collimated jet experiment. Figure 3.6 shows renderings of the experiment done with a CAD program. Targets were machined out of solid acrylic; the bulk of the mass of the target served to anchor the stalk (seen in red in Figure 3.6) and to support the thin cone.

Target	
Material	PMMA $C_5H_8O_2$
Solid density	$1.18\,\mathrm{g\,cm^{-3}}$
Cone opening angle	160°
Cone diameter	2 mm
Cone thickness	100 μm
Distance to TCC	3 mm
Drive Beams	
Drive beam wavelength	351 nm (3ω)
Number beams	7 per cone
Total drive energy	3150 J
Drive beam shape	1 ns, square
Drive beam radius	352 μm (SG4)
Drive irradiance	$8 \times 10^{14}\,\mathrm{W\,cm^{-2}}$
2ω Thomson beam	
Wavelength	526.5 nm
Energy	120 J
Shape	3 ns, square
Radius	70 μm (best focus)
Angle between probe and collector	116.8°

Table 3.2: Experimental parameters for April 2012.

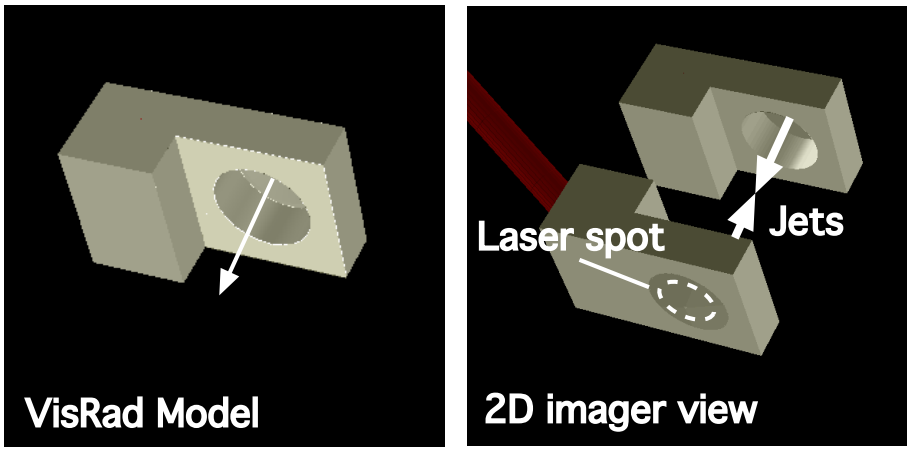

Figure 3.6: CAD renderings of the targets from April 2012 as seen from the point-of-view of the 2-D imager.

3.4 2-D Image Results and Analysis

Out of nine shots, we gained clear images of single jets on two shots and of colliding jets on three shots. For the remaining four shots, the jet was moving away from the imager and the target itself blocked the view. From a technical standpoint, these images were successful (they are in focus), but they contain nothing useful; they can be seen in Appendix C, which contains all of the data from this shot day. The visible light images prove that we were successful in creating collimated jets and that these jets formed well-defined shock structures when collided head-on.

The emission seen in the visible light images is free-free self-emission, or bremsstrahlung, wherein a free electron passes a free ion and has its path diverted. The electron loses kinetic energy in this encounter and to conserve overall energy a photon is emitted.

When this experiment was designed, the jets were expected to have a temperature of $\sim 10\,\mathrm{eV}$, which would make their blackbody spectra peak around 25 nm. In the colliding jet configuration, the shocked material would have a temperature of $\sim 80\,\mathrm{eV}$ and a blackbody peak of 3 nm. Despite these radiation peaks being in the far ultraviolet and soft x-ray, respectively, we chose to image the experiment in the optical. Systems for magnifying and focusing images in the optical are vastly easier to build than similar systems for x-rays and resultantly OMEGA has an optical light imaging system.

3.4.1 Single Jets

Figure 3.7 shows the two successful single-jet images as well as Computer Aided Design (CAD) renderings of the target for reference.

In Figure 3.7, single jets are visible emerging from the counterbore. Some of the features seen in the visible light images in Figure 3.7 are edges of the target: the inner edge of the counterbore is glowing, as well as the surface of the target facing

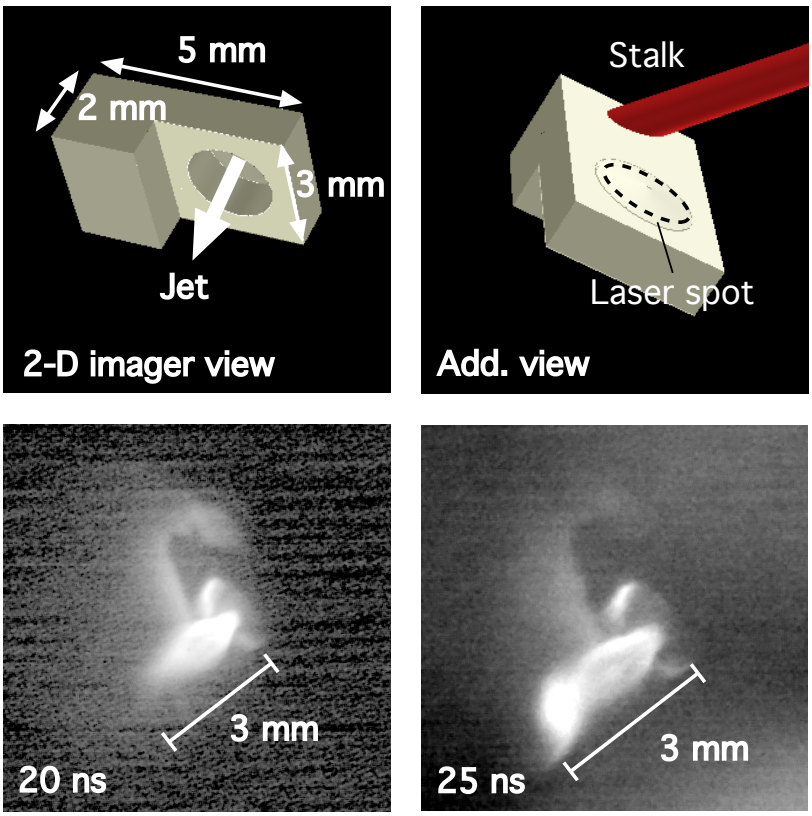

Figure 3.7: Single jet self-emission images from April 2012. Above: CAD renderings of the targets for reference. Below: Self-emission images of jets emerging from targets at 20 ns and 25 ns after drive.

the jet. Although we were interested in the rear-surface rarefaction, when a target is irradiated it completely vaporizes and rarefactions expand from both of its surfaces. Thus, this experiment produced both a rear-surface rarefaction, which was responsible for the collimated jet, and a front-surface rarefaction, which appears in the image as an indistinct background halo.

Figure 3.7 shows well-collimated jets. In the images, the edge of the jet appears brightest. This agrees with the analysis of Section 3.2, which shows that a surrounding shock structure collimates the jet. Figure 3.7 also shows the tip of the jet broadening between 20 ns and 25 ns. This could be the tip of the jet escaping the region where the collimation effects of the cone are still felt and beginning to broaden. I estimate that at their widest, the jets seen in Figure 3.7 were roughly 1 mm in diameter.

3.4.2 Colliding Jets

Figure 3.8 shows colliding-jet images. Figure 3.7 (single jets) is useful for orientation here. Both targets are used in the colliding jet shots, the target used in Figure 3.7, and an additional target is placed in opposition to it. The glow in the foreground is coming off the near side of the near target. This is the front surface irradiation discussed above; with the near target involved in the experiment, it is visible. The laser spot is marked in the CAD rendering in Figure 3.8. Behind that the sides of the near target are dark, and behind one can see the jet from the near target emerging (moving away from the viewer) and the jet from the far target coming to meet it.

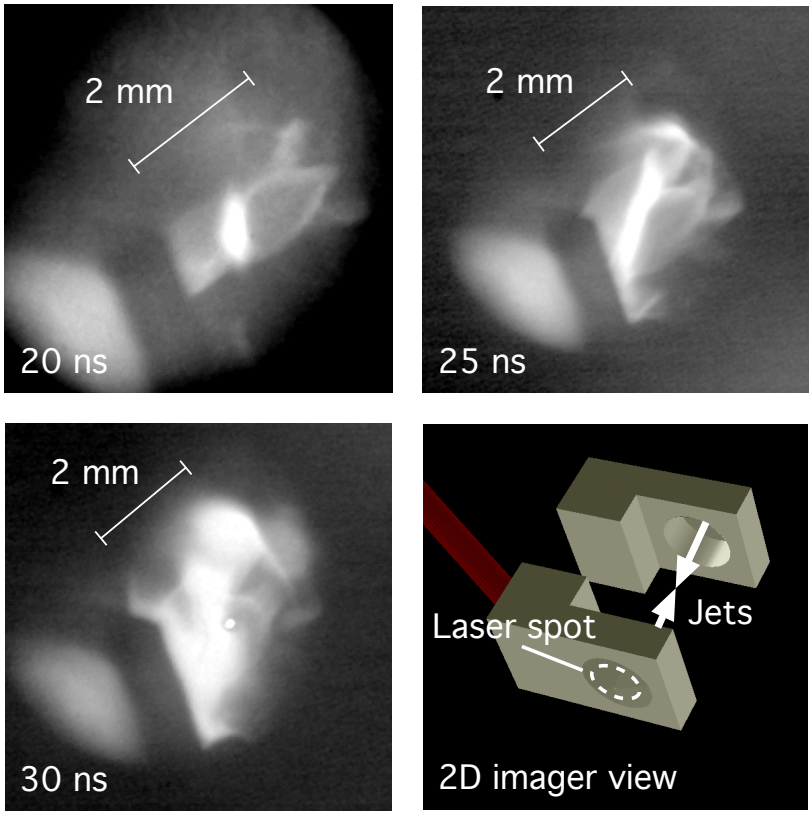

Figure 3.8: Colliding jet self-emission images from April 2012. Above and bottom left: Self-emission images of colliding jet shots at 20 ns, 25 ns, and 30 ns after drive. A bright, shocked region is visible that grows with time. Bottom right: CAD renderings of both targets together.

In the 20 ns image, there is a bright area of shocked plasma where the jets meet.

Unfortunately, we did not take an earlier image, so there is no way to know how early this shock forms. However, judging from how quickly the shocked region appears to grow in the 25 ns and 30 ns images, the shock cannot have been there long in the 20 ns image. This suggests the leading edge of the material forming the shock is moving somewhat faster than $3\,\mathrm{mm}/20\,\mathrm{ns} \sim 150\,\mathrm{km\,s^{-1}}$.

3.5 Thomson Scattering Results

3.5.1 Velocity, Temperature and Density Data

Streaked 2ω (526.5 nm) Thomson scattering, the method employed here, uses a long probe pulse, in our case 3 ns. We staggered the timing of the Thomson probe beam between shots to gain data over extended amount of time. Firing the probe beam from 7 ns to 10 ns did not return any scattered spectra; if any plasma had reached 3 mm at that time, it was not dense enough to scatter the probe beam. Good data was obtained from 12 ns to 15 ns and from 15 ns to 18 ns. We conducted one shot from 20 ns to 23 ns, but the probe beam reflected uselessly off the plasma, a sign that density was approaching the critical density (see Appendix A).

Figures A.8 and A.9 show examples of scattered Thomson spectra extracted from a single-jet experiment 13.5 ns after drive. Both the Electron Plasma Wave or EPW, and the Ion Acoustic Wave, or IAW, are driven by electron density fluctuations. The EPW is the case where the ions are stationary and the electron oscillate; the IAW is the case where the ions oscillate and thereby force the electrons to oscillate as well, see Appendix A for a complete derivation.

The EPW data, seen in Figure A.8, show the intensity falling to zero in between the two peaks. This is artificial; the EPW set-up uses a beam blocker to block wavelengths around the probe beam (526.5 nm).

Every experimental spectrum obtained was hand fit using the spectrum generator

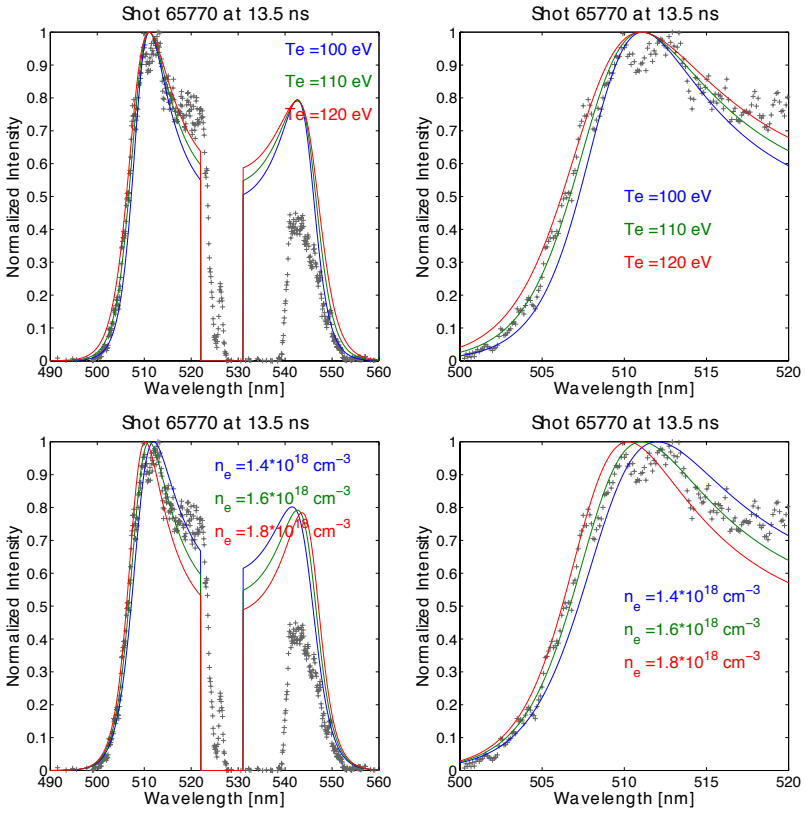

Figure 3.9: Fitting EPW data. Single jet spectrum taken 13.5 ns after drive. Above: the full spectrum with three potential T_e values (left) and zoomed view of the higher peak (right). Below: the full spectrum with three potential n_e values (left) and zoomed view of the higher peak (right). This spectrum (taken 13.5 ns after drive) had the best fit with $T_e = 110\,\text{eV}$ and $n_e = 1.6 \times 10^{18}$.

included in *Froula et al.* (2011), which is explained in detail in Appendix A. The spectrum generator uses electron number density, n_e, electron temperature, T_e, ion temperature, T_i, and velocity, v_a, as inputs and these are varied until a close fit is obtained, see Figures A.8 and A.9. The electron plasma wave spectrum is used to determine n_e and T_e, while the ion acoustic wave spectrum is used to determine v_a and T_i. As seen in Figure A.9, the IAW spectra were not clear enough to distinguish between different values of T_i; therefore data for T_i are not included here.

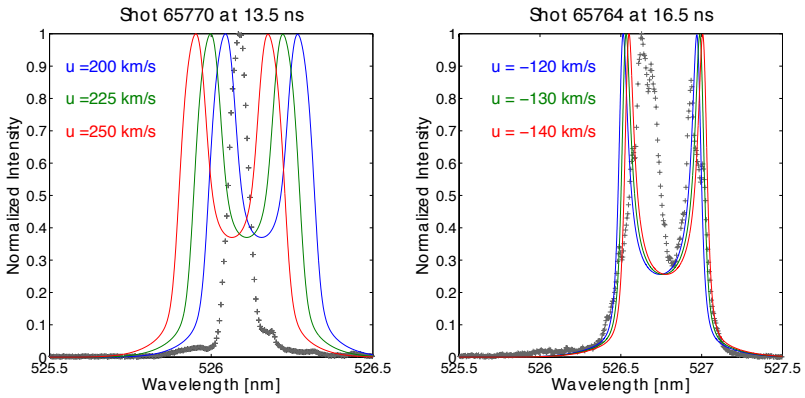

Figure 3.10: Fitting IAW data. Many IAW appeared to have erroneous peaks due to reflected light, but velocity data could still be obtained by fitting the Doppler shift. Left: the IAW data corresponding to Figure A.8. Right: One of the clearest examples of a IAW data we obtained.

Figure 3.11 presents electron density, electron temperature, velocity, and mass density data for the five single jet shots for which Thomson scattering was successful. The error bars for n_e, T_e, and v_a seen in Figure 3.11 were customized for each individual time-specific spectrum; they represent the limits of passable fitting as shown for example in Figures A.8 and A.9.

Of the four parameters shown in Figure 3.11, the first three were directly obtained from the Thomson data, but the fourth, mass density, was calculated according to

$$\rho = n_i A m_p = \frac{n_e A m_p}{Z(T_e)}, \tag{3.4}$$

where A is the average ion mass in proton masses, m_p is the proton mass, and Z is the average ionization. Average ionization is a function of temperature and was obtained by solving the Saha equation (*Drake*, 2006)

$$Z_{\text{bal}} = \sqrt{\frac{k_B T_e}{E_H}} \sqrt{\ln\left[\frac{1}{n_e}\frac{g_j}{4 g_k a_o^3}\left(\frac{k_b T_e}{\pi E_H}\right)^{3/2}\right]} - \frac{1}{2}, \tag{3.5}$$

where Z_{bal} is the average ionization assuming recombination balance, k_B is the Boltzmann constant, E_H is the hydrogen ionization energy, g_j and g_k are the statistical weighting factors for states j and k (we assumed $g_j = g_k$), and a_o is the Bohr radius. Since our temperatures are already in energy units, we have

$$Z_{\text{bal}} = \sqrt{\frac{[T_e\,\text{eV}]}{13.6}} \sqrt{\ln\left[\frac{1}{4 n_e a_o^3}\left(\frac{[T_e\,\text{eV}]}{13.6\pi}\right)^{3/2}\right]} - \frac{1}{2}. \tag{3.6}$$

As seen in Figure 3.11, electron number density ranges from 10^{17} cm^{-3} to 10^{19} cm^{-3}; electron temperature ranges from 50 eV to 400 eV, velocity ranges from 300 km s^{-1} to 100 km s^{-1}, and mass density ranges from $10^{-6.5}$ g cm^{-3} to 10^{-4} g cm^{-3}.

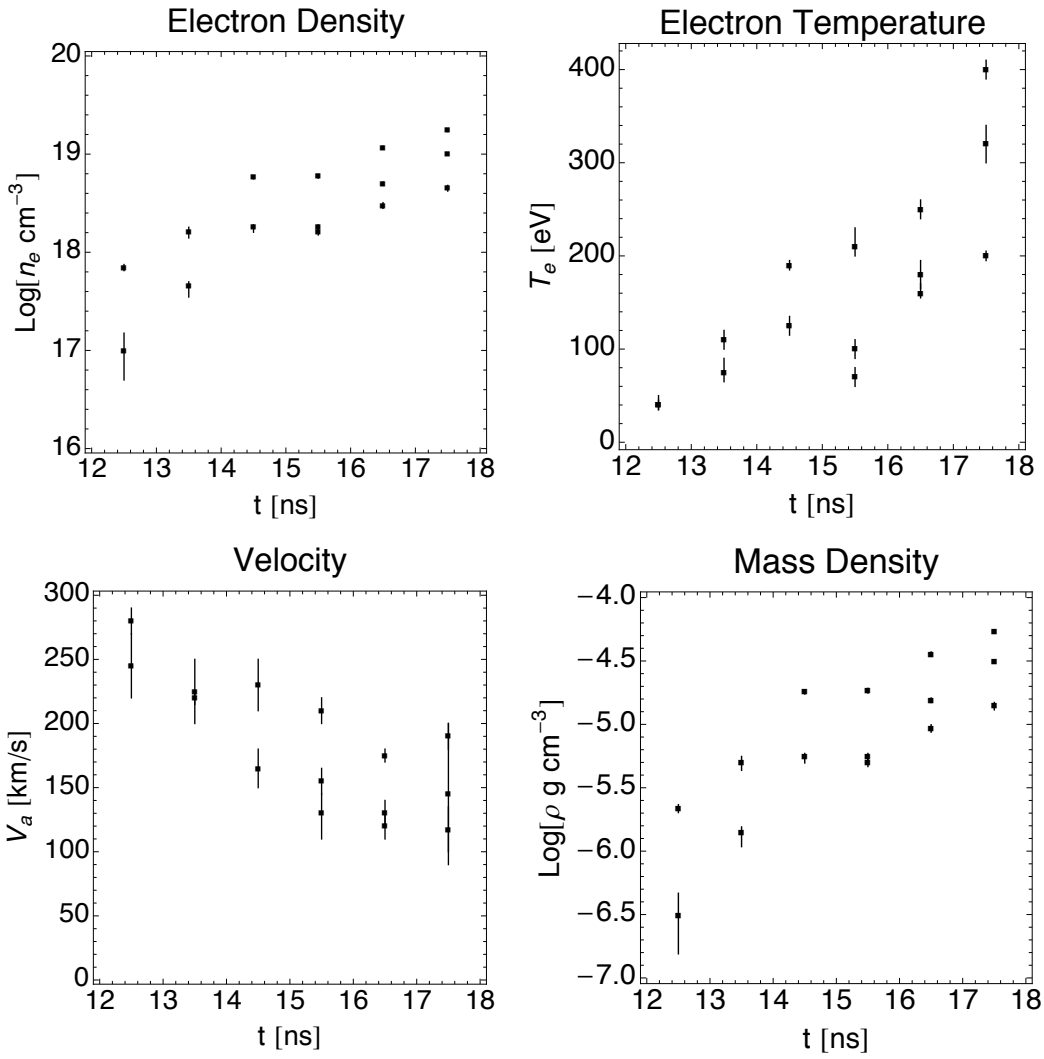

Figure 3.11: Thomson data from April 2012. Electron density and electron temperature increase with time, while velocity decreases. The electron density and temperature numbers are corrupted by probe heating but mass density derived from them ought to be accurate.

3.5.2 Probe Heating

The measured electron temperatures seemed implausibly high—generally temperatures of rear-surface ablations are on the order of 10 eV (*Gregory et al.*, 2008). *Froula et al.* (2011) estimates the increase in plasma temperature due to heating from the Thomson probe beam as

$$\frac{\Delta T_e}{T_e} \simeq 1.28 \times 10^5 \frac{n_i \ln \Lambda}{\omega_i^2 A [T_e]^{5/2}} \int_0^\tau P_i dt, \tag{3.7}$$

where $\ln \Lambda$ is Coulomb lambda, A is the mean ion mass in m_p, and $\int_0^\tau P_i dt$ is the incident power integrated over the pulse length. All quantities in Eq. 3.7 are in CGS units except T_e, which is in eV. See Appendix A for more background on Equation 3.7.

When the plasma parameters from Shot 65770 (the example given in Figures A.8 and A.9) are used in Equation 3.7, the probe heating is estimated as $\Delta T_e/T_e = 8.7$. Moreover, if the original (unheated) T_e were much lower, perhaps $\sim$ 15 eV, then Equation 3.7 would yield $\Delta T_e/T_e = 1300$.

To further investigate the effect of probe heating, I built a simple model, assuming that a plasma with electron density n_e is irradiated by a laser beam with incident wavelength λ_i, incident frequency ω_i, total energy E_{beam}, laser pulse time length τ, and laser beam diameter D. After some distance d, the original intensity, I_o, will be reduced according to

$$I = I_o e^{-\kappa_{\mathrm{EM}} d}, \tag{3.8}$$

where κ_{EM} is the spatial rate of absorption of laser energy (*Drake*, 2006),

$$\kappa_{\mathrm{EM}} = \frac{\nu_{ie} \omega_{pe}^2}{c \omega_i^2} \frac{1}{\sqrt{1 - n_e/n_c}}, \tag{3.9}$$

where ν_{ie} is the ion-electron collisional frequency, ω_{pe} is the electron plasma frequency,

ω_i is the frequency of the incident probe beam, and n_c is the critical density of the plasma. The ion-electron collisional frequency is

$$\nu_{ie} = 3 \times 10^{-6} \frac{n_e \ln \Lambda Z}{T_e^{3/2}} \, \mathrm{s}^{-1}, \tag{3.10}$$

where $\ln \Lambda$ is the Coulomb logarithm, and all quantities are in CGS except T_e, which is in eV (*Drake*, 2006). The electron plasma frequency, taken from the *Plasma Formulary* (*Huba et al.*, 2009), is

$$\omega_{pe} = 5.64 \times 10^4 n_e^{1/2} \, \mathrm{rad\,s}^{-1}. \tag{3.11}$$

The critical density is the electron density at which the electron plasma frequency is equal to the incident laser frequency, $n_c = 1.1 \times 10^{21}/\lambda_\mu^2 \, \mathrm{cm}^{-3}$, where λ_μ is the incident laser wavelength in microns.

For average plasma conditions, $n_e = 10^{18} \, \mathrm{cm}^{-3}$ and $T_e = 15 \, \mathrm{eV}$, the fraction of energy absorbed is low,

$$\frac{I}{I_o} = e^{-\kappa_{\mathrm{EM}}(1 \, \mathrm{cm})} = 0.9913. \tag{3.12}$$

Taking a Taylor expansion, the incident laser energy absorbed by the plasma over length d is $E_{ab} \approx \kappa_{\mathrm{EM}} d E_{\mathrm{beam}}/\tau$.

In the case of the probe heating problem, energy is also lost at the edges of the volume heated by the probe beam due to electron heat flux. Using the free-streaming heat flux model found in *Drake* (2006), which assumes that energy is carried away at the electron thermal velocity, $v_t h$,

$$Q_{\mathrm{FS}} = f_e n_e T_e v_{th}, \tag{3.13}$$

where Q_{FS} has units of energy per area per time, and T_e, once again, is in energy units. The factor f_e is known as the flux-limiter and is usually on the order of 0.1.

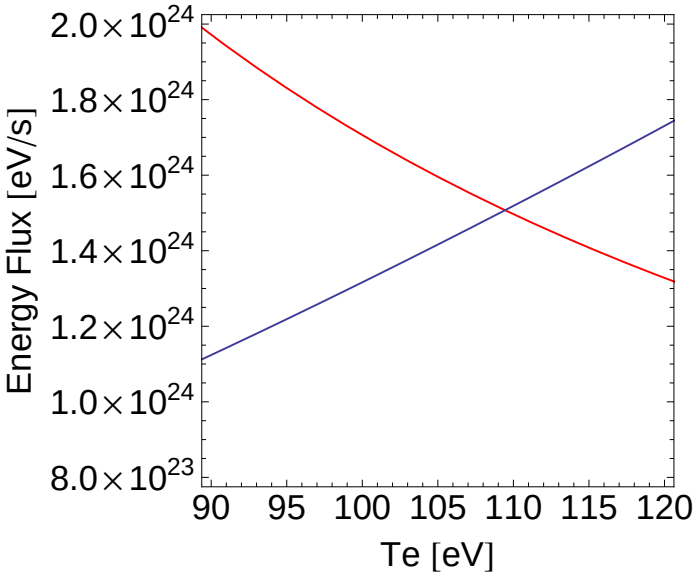

Figure 3.12: Probe energy absorbed by the plasma (red) decreases with temperature, while energy lost increases with temperature (blue).

Consider some cylinder of plasma with diameter D, defined by the focus of the probe beam, and an arbitrary length d. In a steady state, energy rate in is equal to energy rate out.

$$\kappa_{\mathrm{EM}} d \frac{E_{\mathrm{beam}}}{\tau} = f_e n_e T_e v_{th} \pi D d, \tag{3.14}$$

assuming that energy flows out of the cylinder across its sides ($A = \pi D d$) but not across its top or bottom. Figure 3.12 shows the left (red) and right (blue) hand sides of Equation 3.14 plotted for a 527-nm, 3-ns, 120-J probe incident on a plasma with $n_e = 10^{18}$ cm^{-3}. As seen in Figure 3.12, Equation 3.14 has a solution at $T_e = 109\,\mathrm{eV}$.

I solved Equation 3.14 numerically over a range of inputs, fit the solution, and found that the steady-state temperature the plasma reaches can be estimated by

$$T\ [\mathrm{eV}] \approx 145 \left(\frac{E\ [\mathrm{J}]\ n_e\ [10^{18}\ \mathrm{cm}^{-3}]}{\tau\ [\mathrm{ns}]\ D\ [\mu\mathrm{m}]} \right)^{0.345}, \tag{3.15}$$

where T is the temperature, E is the energy of the probe beam, n_e is the electron number density, τ is the time length of the probe beam and D is the diameter of

the probe beam. Substituting the values of this problem, $E = 120\,\mathrm{J}$, $\tau = 3\,\mathrm{ns}$, and $D = 60\,\mu\mathrm{m}$, I found

$$T\,\mathrm{eV} \approx 126(n_e\,[10^{18}\ \mathrm{cm}^{-3}])^{0.345}. \tag{3.16}$$

Figure 3.13 compares the electron temperatures predicted by 3.16 (a function of electron density) and the electron temperatures taken directly from the Thomson data. The dashed line indicates perfect agreement between expected temperatures found with 3.16 and the Thomson-measured temperatures. In general, there seems to be agreement. The simple model in Equation 3.14 predicts the measured temperatures reasonably well. This substantiated the contention that the measured temperature data are the result of probe heating; they do not reflect the plasma conditions before the probe turned on.

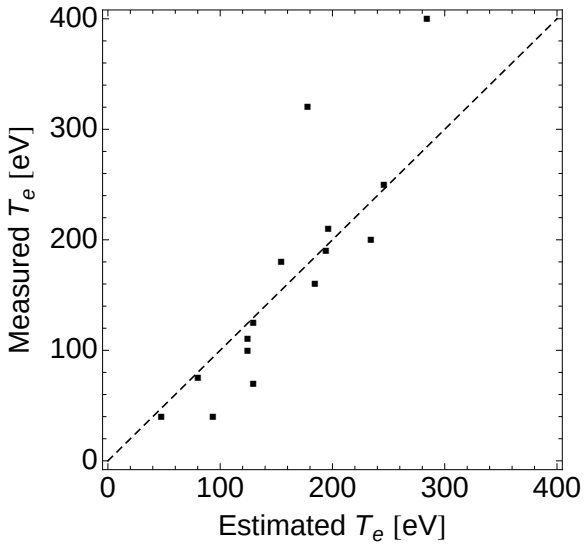

Figure 3.13: Probe heating model predictions vs. measurements. Measured T_e (from Thomson data) agree with temperatures predicted by the probe heating model, Equation 3.16.

3.5.3 Isothermal Rarefactions

A great deal of physical understanding can be gleaned from the mass density data in Figure 3.11. By comparing the data to analytical expressions for rarefactions, I

was able to determine that the jets were behaving as isothermal rarefactions and infer their temperature.

A rarefaction forms when a reservoir of material with some initial density and pressure is released and allowed to expand freely. The material may either cool adiabatically as it expands or it may maintain some constant temperature. If it cools adiabatically, then its density and velocity can be written as

$$\rho(x,t) = \rho_0 \left(\frac{2}{\gamma+1} - \frac{\gamma-1}{\gamma+1}\frac{x}{c_o t} \right), \text{ and} \tag{3.17}$$

$$u(x,t) = \frac{2}{\gamma+1}\left(c_o + \frac{x}{t} \right), \tag{3.18}$$

where ρ_o is the initial density in the pre-expansion plasma, x is the distance from the boundary of the initial reservoir, c_o is the speed of sound in the initial reservoir, and γ is the adiabatic index (*Drake*, 2006). The speed of sound is taken from *Huba et al.* (2009),

$$c_s = 9.79 \times 10^5 \sqrt{\frac{\gamma(Z+1)T_e}{A}}\,\mathrm{cm\,s^{-1}}. \tag{3.19}$$

If, rather than cooling adiabatically as it expands, the rarefaction maintains a constant temperature, it is isothermal and its density and velocity can be written as

$$\rho(x,t) = \rho_o e^{-\left(1+\frac{x}{c_s t}\right)}, \text{ and} \tag{3.20}$$

$$u(x,t) = c_s + \frac{x}{t}, \tag{3.21}$$

where ρ_o, x, and t are the same as in the isothermal case, and c_s is the speed of sound in the system (*Drake*, 2006).

Figures 3.14 and 3.15 compare the mass density and velocity data to analytic predictions for adiabatic and isothermal rarefactions, respectively. For both figures, $\rho_o = 1.18\,\mathrm{g\,cm^{-3}}$, the solid density of CH, and $x = 3\,\mathrm{mm}$, the distance between the

target and the Thomson probe beam. For the adiabatic case, I assumed $\gamma = 1.5$.

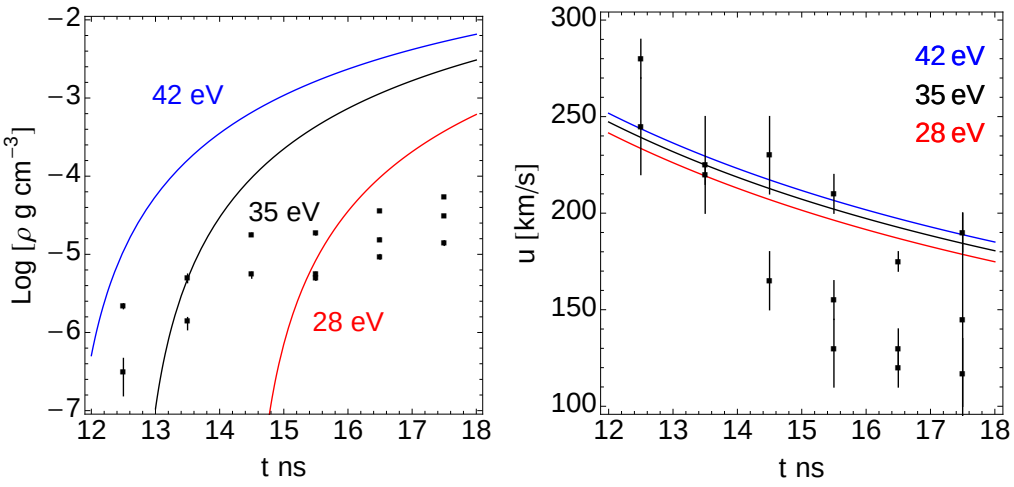

Figure 3.14: Adiabatic rarefactions compared to single jet Thomson data. Density (left) and velocity (right) of adiabatic rarefaction with initial reservoir temperatures of 28 eV, 35 eV and 42 eV. Regardless of the choice of T_o, an adiabatic mass density profile does not match the data.

As seen in Figure 3.14, the basic shape of the adiabatic mass density profile does not match the data and varying the initial temperature does not salvage the situation. The isothermal case, seen in Figure 3.15, is good match. Moreover, because the isothermal density profile is highly sensitive to temperature, I was able to infer the temperature of the jets: 6 ± 1 eV. This is far more reasonable than the previously obtained values of 50 to 400 eV; *Gregory et al.* (2008) measured temperatures of 10 eV for their rear-irradiation-launched aluminum jets.

(I should note, however, that our choice of ρ_o impacts the inferred temperature. If we assume that ρ_o is $10\rho_{\rm CH}$, then the inferred temperature falls from 6 eV to 4.5 eV.)

Velocity profiles, as seen in Figures 3.14 and 3.15, do not change much between the adiabatic and isothermal cases. Neither are they particularly sensitive to temperature. The data show a faster decline in velocity than either the adiabatic or isothermal expression; this is expected of rarefactions expanding into imperfect vacuums.

The isothermal behavior of the jets seems reasonable in light of the electron heat conduction timescale. *Drake* (2011) shows that when t_{equil}/t_{exp} remains small, where

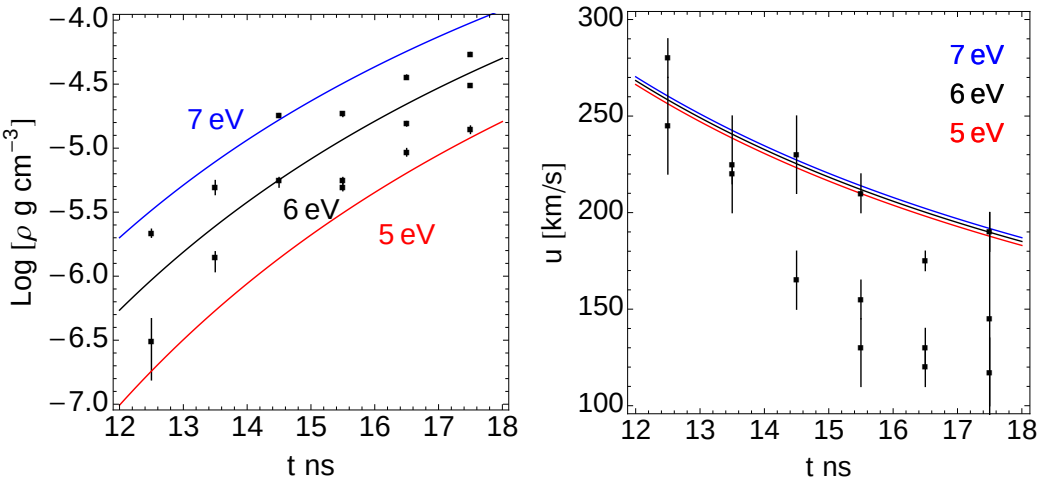

Figure 3.15: Isothermal rarefactions compared to single jet Thomson data. Density (left) and velocity (right) of isothermal rarefactions with temperatures of 5 eV, 6 eV and 7 eV. An isothermal mass density profile with $T_e = 6\,\mathrm{eV}$ matches the data.

t_{equil} is the electron heat conduction timescale and t_{exp} is the experimental timescale, a rarefaction will be isothermal. As conditions approach $t_{equil} \approx t_{exp}$, the rarefaction will transition to adiabatic expansion.

Following *Drake* (2011), the electron heat conduction timescale, t_{equil}, may be found by applying unit analysis to the heat conduction equation, yielding

$$t_{equil} = \frac{\rho C_v L^2}{\kappa}, \tag{3.22}$$

where C_v is the specific heat at constant volume, $C_v = (1 + Z)k_B/(Am_p)$, L is the characteristic length scale, and κ is the heat conduction coefficient. The heat conduction coefficient is defined by

$$\kappa = \frac{128}{3\pi} \frac{n_e k_B T_e}{m_e \nu_{ei}} k_B, \tag{3.23}$$

where ν_{ei} is the electron-ion collision rate, defined as

$$\nu_{ei} = 3 \times 10^{-6} \ln \Lambda \frac{n_e Z}{T_e^{3/2}}\,\mathrm{s}^{-1}, \tag{3.24}$$

where $\ln\Lambda$ is the Coulomb logarithm and T_e is in eV. Thus, the heat conduction equilibrium timescale is defined by the density, temperature, material and length scale. Table 3.3 shows the equilibrium timescale calculated for a range of L from 0.1 mm to 1 mm and a range of ρ from 10^{-7} to $10^{-4}\,\mathrm{g\,cm^{-3}}$.

$\rho[\mathrm{g\,cm^{-3}}] \rightarrow$ $L[mm] \downarrow$	10^{-7}	10^{-6}	10^{-5}	10^{-4}
0.1	0.04	0.3	3	20
0.3	0.9	8	60	500
1.0	4	30	300	2000

Table 3.3: Heat conduction equilibrium timescales, t_{equil}, in nanoseconds, for ranges of density and length scale for a CH plasma at 6 eV.

From Table 3.3, $t_{equil} < 10$ ns for low densities and short length scales. Therefore isothermal behavior would be expected at early times, which was the case for this shot day. It would be beneficial to study jets such as these at later times to see if the isothermal behavior endures, but this was precluded on shot day because we reached the density limit of 2ω Thomson scattering.

3.6 Conclusion

The April 2012 shot day was my first day of experiments at OMEGA. Our collaboration was successful in creating collimated plasma jets by rear-irradiating 100 μm-thick CH conical targets. We found the following, which would prove useful in developing the accretion shock experiment later:

1. Both single-jet experiments and colliding-jet experiments show clear signs of collimation in 2D self-emission images.

2. Colliding-jet images show a shock forming between them. This shock was evident in our earliest image (20 ns after drive) and appears to grow with time.

3. Thomson scattering data were corrupted by probe heating, but velocity data were unaffected and mass density data (derived from electron density and temperature) are still accurate.

4. The mass density profile matches that of an isothermal rarefaction with $T_e = 6 \pm 1\,\mathrm{eV}$, giving an alternate approach to temperature measurement in light of our difficulties with probe heating.

CHAPTER IV

Accretion Shock Experiments

Chapter II introduced the scaled accretion shock experiment and concluded that it would be well-scaled if a 10-T field were imposed on a 10-eV CH plasma with $\rho \sim 10^{-5}\,\mathrm{g\,cm^{-3}}$ and $u \sim 100\,\mathrm{km\,s^{-1}}$, *or* if a 30-eV CH plasma with $\rho \sim 3 \times 10^{-6}\,\mathrm{g\,cm^{-3}}$ and $u \sim 150\,\mathrm{km\,s^{-1}}$.

Chapter III presented experiments done to characterize collimated jets made by rear-irradiating thin acrylic cones. It concluded that the jets were behaving like 6-eV isothermal rarefactions with $\rho \sim 10^{-6.5}$–$10^{-4.5}\,\mathrm{g\,cm^{-3}}$ and $u \sim 100$–$250\,\mathrm{km\,s^{-1}}$.

This chapter presents the results of the accretion shock experiment, which used jets similar to those developed in Chapter III to accomplish the experimental concept articulated in Chapter II. Section 4.1 presents the experimental set-up. To translate this system into a laboratory experiment, I designed an experiment with an incoming plasma jet (the "accreting flow"), an impact surface for it to collide with (the "stellar surface") and a surrounding magnetic field which ran parallel to the jet velocity and perpendicular to the impact surface.

This experiment used two primary diagnostics: 2-D visible light imaging (the technique employed successfully for the collimated-jet experiments in Chapter III) and proton radiography. Section 4.2 presents the visible light data of the accretion shock experiment. The data show a jet clearly emerging, meeting the impact surface

and creating a bright shock structure.

Section 4.3 puts the accretion shock visible light data into context by comparing it to the collimated jet visible light data from Chapter III. The experiments are similar; the collimated jets collided head-on with each other, while the accretion shock jet collides with a wall.

Section 4.4 revisits the scaling argument made in Chapter II, and Section 4.5 presents my conclusions.

Unfortunately, while proton radiography was intended to be a primary diagnostic, we encountered repeated difficulties with it and were never able to obtain conclusive data. This is discussed in full in Chapter V.

4.1 Experimental Set-up

To scale an accretion shock to a laboratory experiment requires both reproducing the basic elements of the astrophysical system and tailoring the plasma parameters to preserve its physics. Scaling concerns for the actual experiment, as opposed to the ideal experiments presented in Chapter II, are discussed in Section 4.4. This section discusses the configuration of the experiment, which required an incoming plasma jet (the "accreting flow"), an impact surface (the "stellar surface") for it to collide with, and a surrounding magnetic field which ran parallel to the jet velocity and perpendicular to the impact surface, see Figure 4.1.

As seen in Figure 4.2, rear irradiation launches a single plasma jet, which travels "down" to collide with the impact surface "below." (Because the experiment lasts less than 100 nanoseconds, gravity does not play a significant role; in the target chamber it does not matter which way is literally down. I have used the terms "down" and "below" to emphasize the connection to the astrophysical system of Figure 4.1.) The experiment is suspended inside two MIFEDS current coils. Beginning before the shot is fired, the high-voltage MIFEDS capacitors discharge through the wire loops, shown

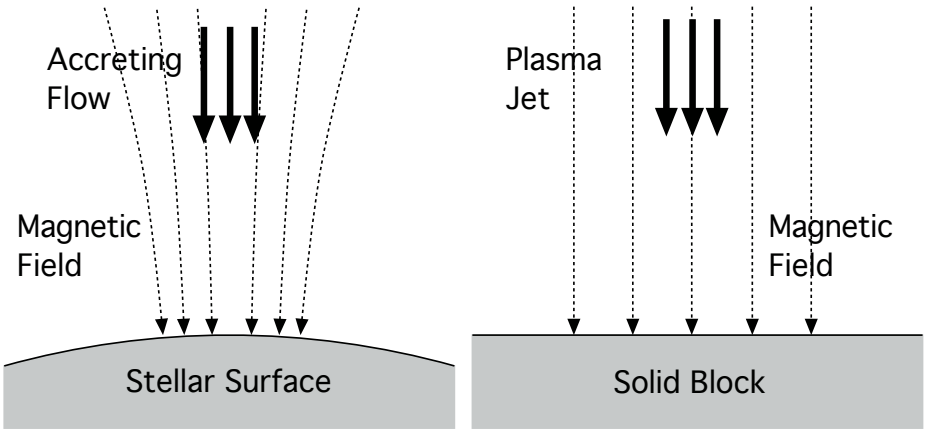

Figure 4.1: Translating the astrophysical system to the lab. This requires a plasma flow, magnetic field and impact surface.

in 4.2 in cross-section. See Appendix A for more information on MIFEDS.

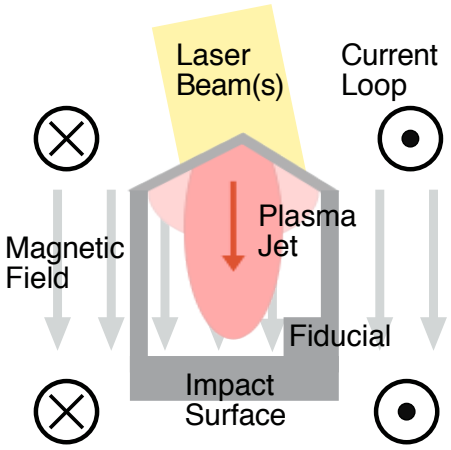

Figure 4.2: Schematic for the accretion shock experiment.

The accretion shock target, seen in Figure 4.3, was entirely constructed from acrylic and was micro-machined in-house at the University of Michigan, like the collimated-jet targets from Chapter III. The target was made in two pieces: a large acrylic block with two walls protruding from it on one end and an acrylic "roof," with a thin cone machined into it, that rested on the walls.

The two primary diagnostics for this experiment were visible light imaging and proton radiography. We failed to obtain conclusive data for proton radiography; Chapter V or Appendix B discusses this in full.

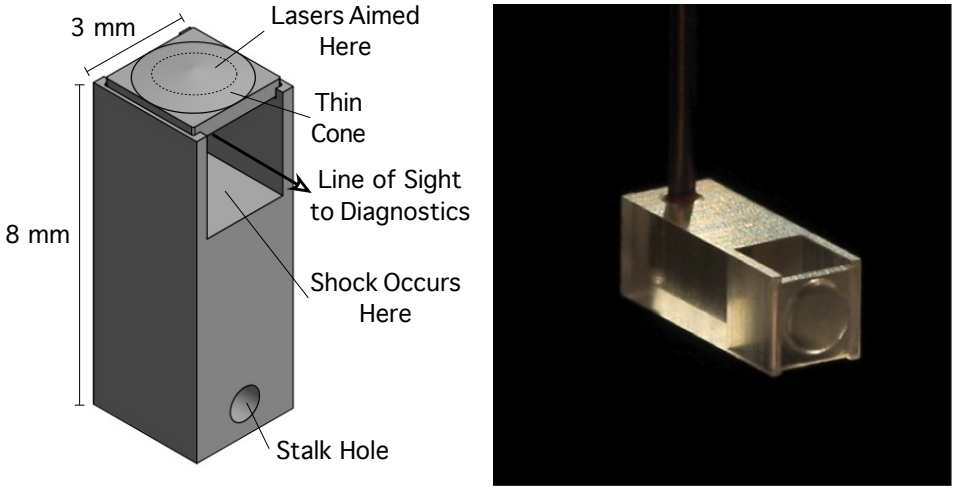

Figure 4.3: Engineering rendering and photograph of the accretion shock target. Both the drawing and the photo are of 2014 targets; it lacks the fiducial that was added for the 2015 shot days.

Figure 4.4 shows CAD renderings of the accretion shock targets in the target chamber and it highlights one of the fundamental difficulties of imaging this experiment. The target must be maneuvered inside the current coils and behind the proton backlighter and its associated shield, which protects the imaging system from the backlighter blast. Thus there at least three things potentially standing between the experiment and the imager: the coils, the backlighter, and shield protecting the backlighter. The experiment is designed to give the imager a clear line of sight, but if any of these things shift unexpectedly data could be lost.

Table 4.1 provides a summary of experimental parameters. As seen in Table 4.1, the accretion shock experiment was done with either one or seven drive beams launching the plasma jet. For the 2014 shot day, we used seven beams consistent with the collimated jet work of Chapter III. For the 2015 shot days, we dropped down to one drive beam in an attempt to reduce the density and velocity of the incoming jet and thereby improve the scaling of the experiment. The ramifications of this are discussed in Section 4.4.

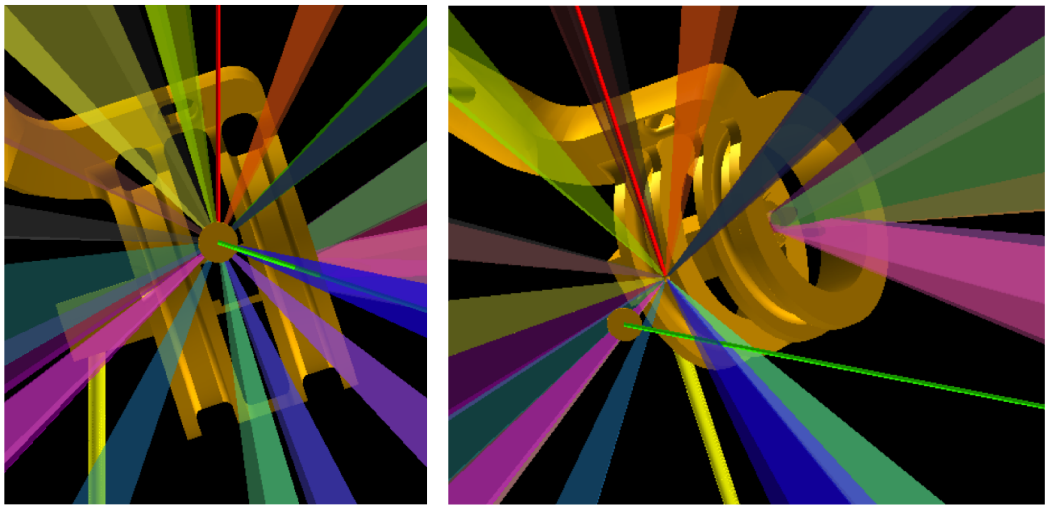

Figure 4.4: CAD views of the accretion shock experiment. A view from the perspective of the visible light imager on the left and a generic view on the right. Note the similarity to the 2014 experiment; the addition of the shield (the gold disk on the green stalk) is the only obvious difference in this view.

4.2 Visible Light Data

Figure 4.5 shows all the visible light data from the accretion shock experiment. These images were taken using the 2-D imager that performed so well for the collimated jet work of Chapter III). As with the collimated jet images, the system was gated to 3 ns and a long pass filter was used to block the drive beam frequency ($\lambda < 385$ nm) along with one or more neutral density filters. Appendix A contains more detail on the visible light imager and Appendix B lists the filtering for each shot.

Shots 77250 and 77251 were used to get filtering right. Shot 77254 was a control and Shot 77255 was the first good experimental data. After Shot 77255, we decided to reduce the laser intensity by dropping from seven beams to one in order to reduce the density and velocity of the incoming jet.

The top two rows (Shots 77250 to 77259) had MIFEDS inserted into the chamber to impose a magnetic field, while the bottom row did not. The effect of MIFEDS on the visible light images is easiest to see by observing 77254, a control shot for

Target	
Material	PMMA
Solid density	$1.18\,\mathrm{g\,cm^{-3}}$
Cone opening angle	160°
Cone diameter	2 mm
Cone thickness	$100\,\mu$m
Drive Beams	
Drive beam wavelength	351 nm (3ω)
Number beams	7 or 1
Total drive energy	3150 J or 450 J
Drive beam shape	1 ns, square
Drive beam radius	$352\,\mu$m (SG4)
Proton Backlighter Beams	
BL beam wavelength	351 nm (3ω)
Number beams	15 (2014) or 18 (2015)
Total drive energy	6750 (2014) or 8100 (2015) J
BL beam shape	1 ns, square
MIFEDS	
Type of field	Parallel
Max field strength	7 T

Table 4.1: Experimental parameters for the accretion shock experiments. The makeup shots in October 2015 shots were the same as the May 2014 and May 2015 experiments, except the MIFEDS and proton backlighting were dropped. Appendix B gives a complete synopsis of this.

which the drive beam(s) were not fired. Ideally, 77254 would be completely dark and neither MIFEDS nor proton radiography would produce light to interfere with the experimental image. Instead, the image for Shot 77254 shows glowing shapes above and below the experimental region—either the MIFEDS coils are glowing or they are reflecting light from the proton backlighter. There is also a dark shape cutting across the top left corner; this is the stalk that supported the visible-light-system shield mentioned in Section 4.1. These glowing shapes above and below the experimental volume are seen on all of the other shots for which MIFEDS and proton radiography were used, Shots 77254 through 77259.

The best visible light data obtained were the two time-series of shots, with and without an imposed magnetic field. The magnetic-field shots (middle row of Figure

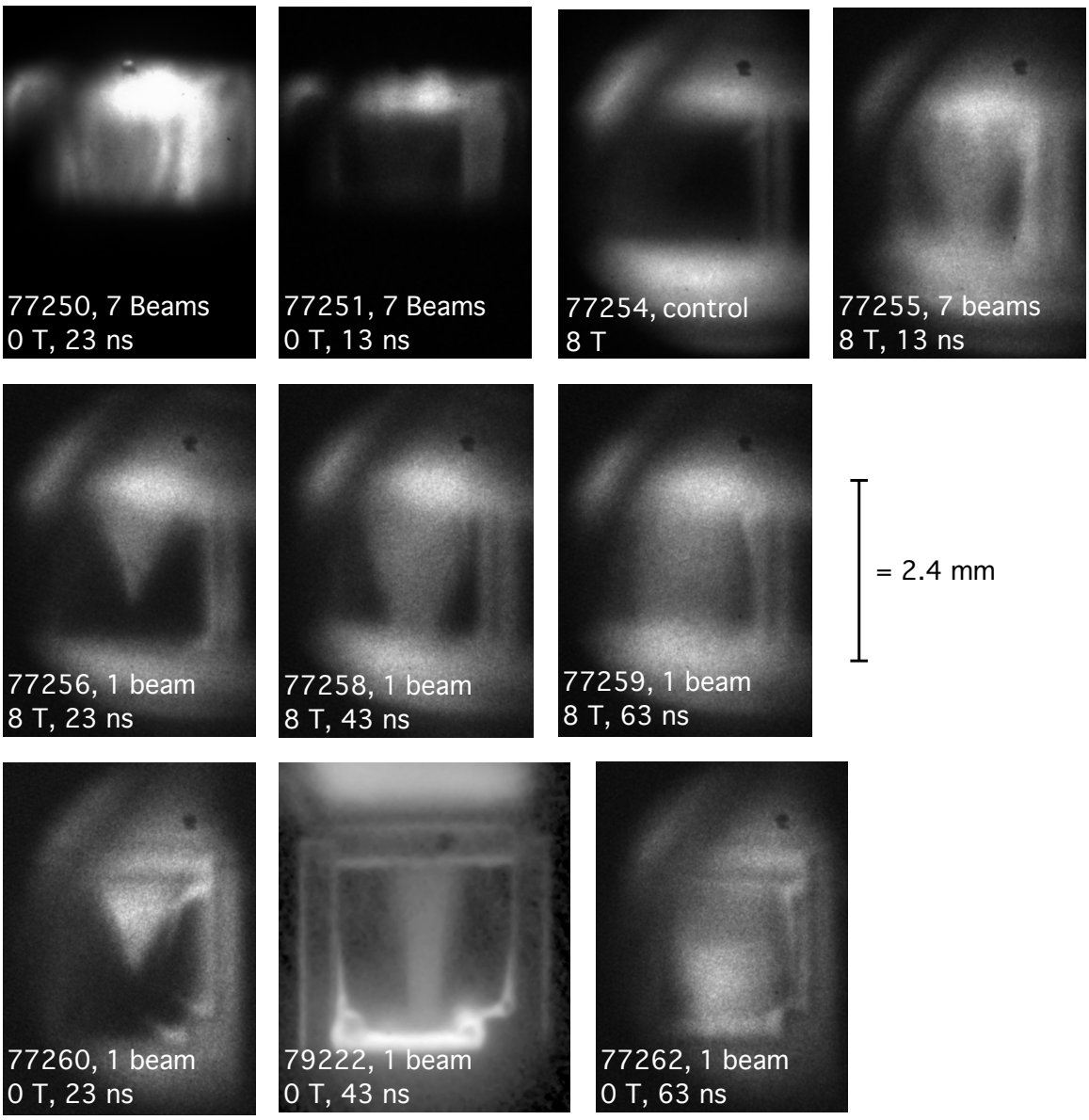

Figure 4.5: All visible light data from the accretion shock experiment. The top row shows initial shots used to establish experimental parameters such as number of drive beams and timing. The middle and bottom row each show a time series of shots either with a magnetic field (middle row) or without (bottom row).

4.5) and the no-field shots (bottom row of Figure 4.5), show some obvious differences because they were taken with slightly different configurations. The magnetic-field shots used MIFEDS, while the no-field shots did not. Thus, the no-field shots lack the glowing shapes above and below the experimental volume.

The fiducial, illustrated in Figure 4.2 and seen in the CAD renderings of Figure 4.4, is clearly visible in all three no-field shots, but is not evident in the magnetic-field shots. This is troubling; the experiment was designed such that the fiducial ought to have been visible with or without MIFEDS in use. Its disappearance suggests that the MIFEDS coils might have been squeezing together when the current was driven through them and thereby obscuring part of the experimental volume. This is plausible; MIFEDS wires are bent completely out of shape when the coil is fired, see Figure 4.6. Finally, the viewer will notice that Shot 79222 has a much crisper image than all of the other shots. Shot 79222 is a makeup shot from October 2015; no proton radiography was used and all the neutral density filters were removed, so the imager was able to capture more detail.

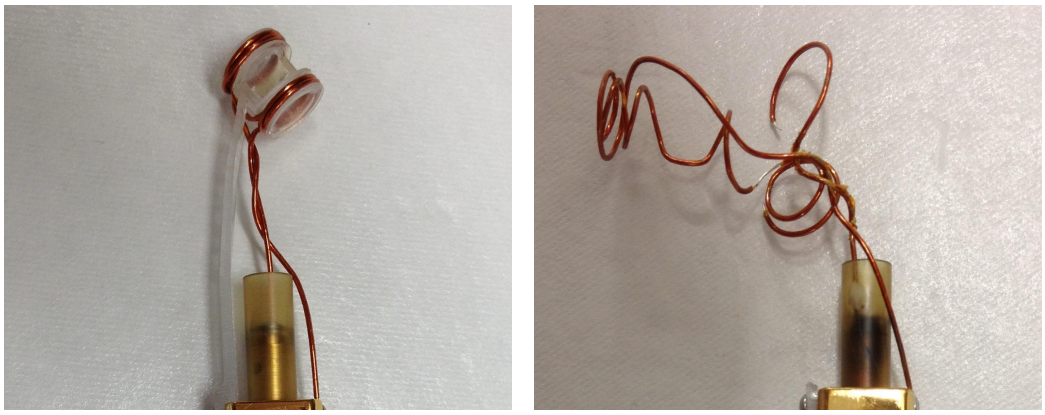

Figure 4.6: A typical MIFEDS coil before being fired (left) and after (right). This project used a similar design to the MIFEDS device pictured above; while the above device has a thin wall of plastic connecting the upper and lower coils, the accretion shock design did not. (Image credit: Sallee Klein)

Beyond the differences in experimental set-up between the magnetic-field and no-field shots, there is very little observably different between two time series. Both show a jet emerging from the top of the target at 23 ns (Shot 77256/77260), making contact with the impact surface at 43 ns (Shot 77258/79222), and forming a hot, bright region at 63 ns (Shot 77259/77262). Because of the MIFEDS distortion problem discussed above, we cannot see the bottom of the experimental volume in the magnetic field

time series.

Figure 4.7 shows intensity along the center line of two visible light images: Shot 79222, no field at 43 ns, and Shot 77262, no field at 63 ns. At 43 ns, the jet has reached the impact surface. The impact surface is glowing brightly, as seen in the intensity peak at $x = 3\,\text{mm}$ ($x = 0$ is the tip of the cone that launched the jet); this could be a shock just beginning to form or it could be the surface itself glowing after being heated by X-rays. The lineout at 63 ns, however, shows two clear zones of differing intensity, which split at $x = 1.8\,\text{mm}$, where $x = 0\,\text{mm}$ is the original position of the target and $x = 3\,\text{mm}$ is the position of the impact surface. The discontinuity between the two zones is 0.2 mm wide, making the height measurement with error $x = 1.8 \pm 0.1\,\text{mm}$. There is a bright zone near the impact surface, which I conclude is shocked material, and a less bright zone above it, which ought to be unshocked material.

4.3 Shock Evolution

Visible light imaging was used successfully for both the collimated jet campaign and the accretion shock campaign. This section compares the data from both campaigns to better understand the structure of incoming jets in the accretion shock experiment and the evolution of the shocks that formed in both experiments.

4.3.1 Comparisons to Collimated Jets

In April 2012 our experimental team dedicated a day of shots to testing a method for creating collimated plasma jets: rear irradiation of a thin cone of PMMA. As presented in Chapter, III, we launched these jets singly and in head-on collision configurations; the primary diagnostics were Thomson scattering and visible light imaging. Due to probe heating, the temperature data obtained were unreliable. However, I was able to create mass density profiles based on the Thomson data, which I used to determine that the jets were behaving as isothermal rarefactions with $T_e = 6 \pm 1\,\text{eV}$.

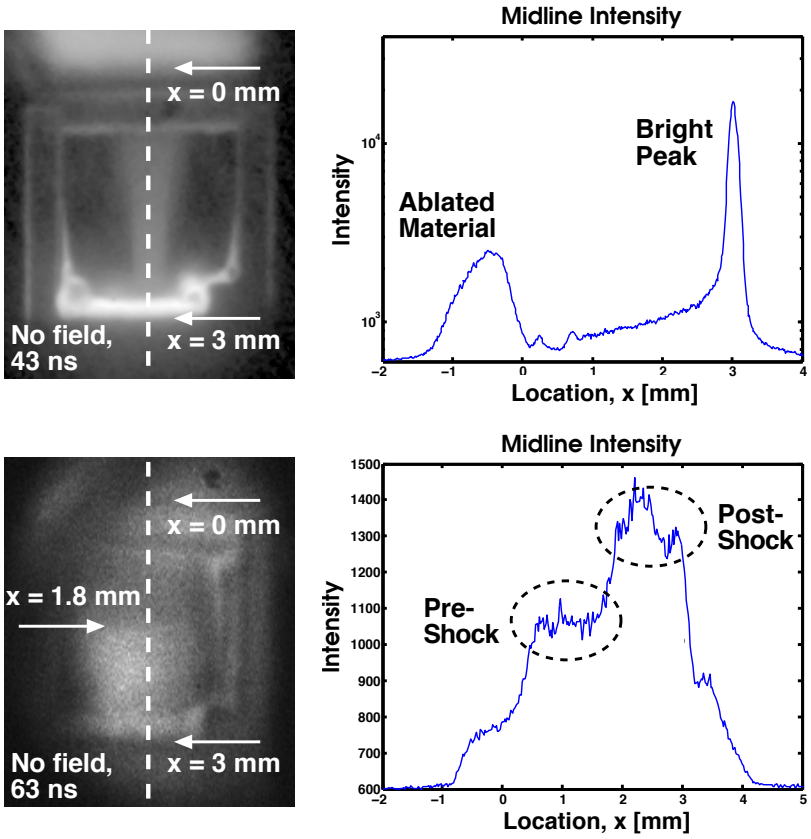

Figure 4.7: Intensity along the midline of the visible light data. The dashed white line in the visible light images (left) indicates where the lineouts were taken; these are plotted on the right. $x = 0\,\text{mm}$ indicates the location of the original target; $x = 3\,\text{mm}$ indicates the location of the impact surface.

As stated in Section 4.1, while we used seven drive beams for the collimated jet shots, we fell back to one drive beam for the second accretion shock shot day. Thus, most of the visible light data are for shots with only one drive beam. These one-beam jets were never probed with Thomson scattering, so their plasma properties must be determined via scaling laws, see Table 4.2. The dependence of temperature on direct laser irradiation intensity is $T_e \propto I^{2/3}$ (*Drake*, 2006), which would make the temperature of the one-beam jets $T_e = (1/7)^{2/3}(6 \pm 1\,\text{eV}) = 1.6 \pm 0.4\,\text{eV}$.

The dependence of ablation pressure on direct laser intensity is $P_{abl} \propto I^{2/3}$ (*Drake*, 2006). Since $P_{abl} \propto u^2$, this yields $u \propto I^{1/3}$. The 23–43–63 ns time series for 1-beam accretion shock experiments would correspond to a hypothetical 12–22–33 ns time

	Collimated Jets	Accretion Shock
Date	April 2012	May/Oct 2015
Jets creation method	rear-irradiation, thin cone	rear-irradiation, thin cone
Cone thickness	100 μm	100 μm
Cone material	acrylic (PMMA)	acrylic (PMMA)
Drive beams	7, full power	1, full power
Configuration	collided head on	collided with solid surface
Distance to collision	3 mm	3 mm
Visible light imager	TPDI	TPDI
Thomson scattering used	yes	no
Jet behavior	isothermal	isothermal*
Jet temperature	6 ± 1 eV	1.6 ± 0.4 eV*

Table 4.2: Comparing the collimated jet experiments and the accretion shock experiments. *The 1-beam jets are assumed to be isothermal like the 7-beam jets and their temperature is inferred from $T_e \propto I^{2/3}$.

series for 7-beam colliding jet experiments. The actual time series taken the colliding jet experiments was 20–25–30 ns, but there is good correspondence between both time series as seen in Figure 4.8.

The earliest accretion shock image, 23 ns, is not equivalent to any of the colliding jet images. The second accretion shock image, 43 ns, would be equivalent to 22 ns and resembles the 20 ns colliding jet image. In both images, the jet(s) have just reached the impact surface/collision point. In the colliding jet image, the bright spot at the collision point is clearly a shock—there is nothing else for it to be. In the accretion shock image, it could be a nascent shock structure forming or it could be the impact surface itself glowing. If it is a shock, it has just formed. The final accretion shock image, 63 ns, would be equivalent to 33 ns for the 7-beam case and resembles the 30-ns colliding jet image. There is a bright volume of shocked material in both, although it is harder to see its outline clearly in the colliding jet work because those images were taken from an angle.

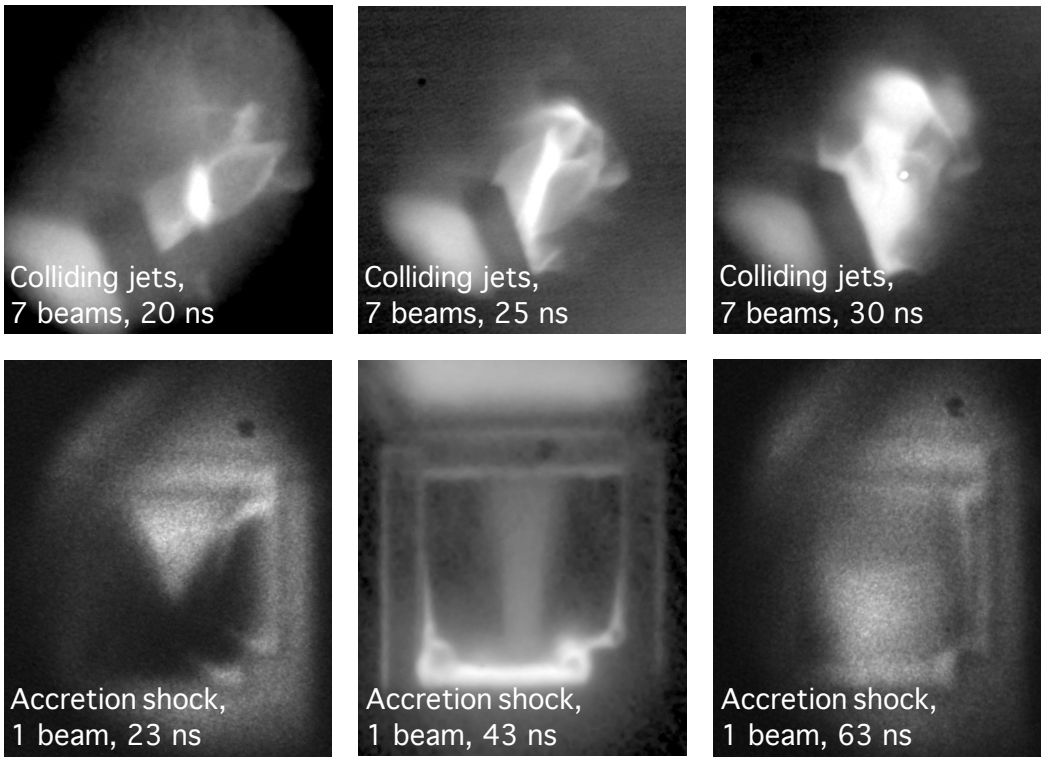

Figure 4.8: Comparing the collimated jet experiments (above) and the accretion shock experiments (below). These images have been rotated, cropped, and adjusted for brightness.